Research Article

Nano Research
2023, 16(2): 3240–3253

ISSN 1998-0124 CN 11-5974/O4
https://doi.org/10.1007/s12274-022-5062-3

"One stone, two birds" solvent system to fabricate microcrystalline cellulose–$Ti_3C_2T_x$ nanocomposite film as a flexible dielectric and thermally conductive material

Yong-Zhu Yan[1], Shuwei Li[2], Sung Soo Park[3], Wei-Jin Zhang[1], Jun Seok Lee[1], Jung Rae Kim[2], Dong Gi Seong[1], and Chang-Sik Ha[1] (✉)

[1] *Department of Polymer Science and Engineering, School of Chemical Engineering, Pusan National University, Busan 46241, Republic of Korea*
[2] *School of Chemical and Biomolecular Engineering, Pusan National University, Busan 46241, Republic of Korea*
[3] *Division of Advanced Materials Engineering, Dong-Eui University, Busan 47340, Republic of Korea*

Received: 22 June 2022 / **Revised:** 16 September 2022 / **Accepted:** 16 September 2022

ABSTRACT

A strategy for fabricating microcrystalline cellulose–$Ti_3C_2T_x$ (MCC–MXene) nanocomposite films with high relative permittivity, high thermal conductivity, and excellent mechanical properties was developed. The MCC–MXene nanocomposite film was fabricated by casting a solution containing N,N-dimethylacetamide/lithium chloride (DMAc/LiCl)-soluble MCC and DMAc-dispersible MXene nanosheets, followed by humidity control drying. The MXene nanosheets greatly enhanced the permittivity of the nanocomposite films owing to interfacial polarization. Thus, the nanocomposite film with 20 wt.% MXene content achieved a desirable permittivity of 71.4 at 10^2 Hz (a 770% improvement against that of neat cellulose), while the dielectric loss only increased by 1.8 times (from 0.39 to 0.70). The obtained nanocomposite films with 20 wt.% and 30 wt.% MXene exhibited remarkable in-plane thermal conductivities of 8.523 and 9.668 $W \cdot m^{-1} \cdot K^{-1}$, respectively, owing to the uniform dispersion and self-alignment of the MXene layered structure. Additionally, the uniformly dispersed MXene nanosheets in the MCC network with interfacial interaction (hydrogen bonding) and mechanical entanglement endowed the nanocomposite films with excellent mechanical properties and flexibility. Furthermore, the thermal stability, water resistance, and antibacterial properties of the nanocomposite films were effectively improved with the introduction of MXene. Moreover, using DMAc/LiCl as the solvent system not only improves the compatibility between MCC and MXene but also avoids the problem of easy oxidation of MXene in aqueous systems. With the high stability of the MCC–MXene solution and enhanced properties of the MCC–MXene films, the proposed strategy manifests great potential for fabricating natural biomass-based dielectric materials.

KEYWORDS

$Ti_3C_2T_x$, microcrystalline cellulose, flexible dielectric, thermally conductive, N,N-dimethylacetamide/lithium chloride (DMAc/LiCl), compatibility

1 Introduction

With the rapid development of modern electronic and power systems, there is an urgent demand for polymer-based electrical materials possessing both a high dielectric constant and low dielectric loss in the production of electrostatic film capacitors with high energy density, owing to their flexibility and ease of processing [1–6]. In addition to having a high dielectric constant, efficient heat dissipation is also important for the practical application of dielectric materials. The reliability of electronic devices is related to the operating temperature. To ensure high performance and reliability of these devices, ideal high dielectric constant materials should also possess high thermal transport capability to meet thermal management requirements. Therefore, there is a great need to develop polymer composites with both high dielectric constants and thermal conductivities [7–9].

A variety of polymeric materials, such as poly(methyl methacrylate) [10], polyacrylonitrile [11], polyimide [12], poly(4-vinylphenol) [13], and poly(vinyl alcohol) (PVA) [14], used as matrix materials have been applied as dielectric materials in electronic devices. However, as these synthetic polymers are not biodegradable and renewable, they can lead to serious environmental problems. Biomass materials such as sodium alginate and cellulose have recently attracted a lot of attention as environmentally sustainable solutions that can enable unprecedented advances in various energy storage devices [15–17]. Among the various biomass-based, natural, and environmentally friendly materials reported so far, cellulose and its derivatives have been considered important because cellulose is naturally inexhaustible and has the advantages of biocompatibility, recyclability, low cost, and lightweight [18]. Furthermore, the abundant hydroxyl groups in cellulose tend to form a larger proportion of intermolecular hydrogen bonds with functionalized nanofillers, which is beneficial for obtaining homogeneous nanocomposite materials with good mechanical properties [19, 20]. Thus, developing novel cellulose-based materials such as high dielectric and high thermal conductivity materials for electronic devices is of utmost importance.

Address correspondence to csha@pnu.edu

Several common strategies have been proposed to increase the dielectric constant of polymer-based composites. One is introducing a high dielectric constant inorganic ceramic nanofiller, such as $BaTiO_3$ [21], ZrO_2 [22, 23], TiO_2 [24], and copper calcium titanate [25], into the polymer matrix. However, the use of ceramic nanofillers for fabricating flexible electronic devices is disadvantageous because large amounts of ceramic fillers are necessary, and their inherent brittleness causes the composite material to break easily [26]. Another approach is to prepare electrical percolative composites by using conductive fillers, including reduced graphene oxide (rGO) [27], carbon nanotubes [28], $Ti_3C_2T_x$ (MXene) [29, 30], and silver nanowire (AgNW) [31]. Conductive nanomaterials can provide many microscopic dipoles and microcapacitor networks extending into the entire insulating polymer matrix, thereby enhancing the dielectric properties of polymer nanocomposites through interfacial polarization (permeation threshold) at relatively low filler contents [32].

Two-dimensional (2D) conductive MXenes are a promising alternative for electronic miniaturization owing to their nanoscale thicknesses and high aspect ratios. Because of their unique 2D structure and inherent properties, they have numerous advantages such as high electrical conductivities, large specific surface areas, electromagnetic shielding properties, and good thermal conductivities [33–35]. These make them promising materials for capacitors, thermal management systems, electromagnetic shielding devices, etc. Tu et al. demonstrated that poly(vinylidene fluoride)-based nanocomposite materials using 2D MXene nanosheets as fillers exhibit significantly enhanced dielectric constants [36]. Jin et al. prepared PVA/MXene multilayered films that exhibited a high thermal conductivity [37]. Hence, 2D MXene nanosheets can be a candidate for producing nanocomposite materials with high dielectric constants and thermal conductivities. It was reported, however, that $Ti_3C_2T_x$ MXene has an in-plane thermal conductivity of 55.8 $W{\cdot}m^{-1}{\cdot}K^{-1}$, which is not as extremely high as graphene (~ 5,300 $W{\cdot}m^{-1}{\cdot}K^{-1}$) [38, 39]. Furthermore, it is well known that high interfacial thermal resistance at the polymer/filler interface will inhibit the transfer of phonons from the filler to the polymer matrix, which is not conducive to the formation of thermally conducting pathways. And the dispersion state of filler and the interaction with the polymer matrix will affect percolation threshold, thereby affecting the efficiency of thermal conductivity improvement of composites. Therefore, achieving low interfacial thermal resistance is necessary for building high thermal conductivity hybrids with MXene as filler, which gets much minimized by the excellent compatibility, stronger interfacial interaction, and good MXene layered structure arrangement [37, 40]. In addition, considering the hydrophilic characteristic of MXene, MXene nanosheets synthesized by many researchers using a minimally intensive layer delamination (MILD) method are stably dispersed in water systems [41]. Therefore, nanocomposite materials containing MXene fillers are usually synthesized in aqueous systems [42]. Unfortunately, 2D MXenes undergo irreparable surface morphological and structural changes during oxidation, especially in aqueous solutions. Water has been confirmed to be the culprit of MXene oxidation. Many researchers have proposed various methods to protect MXene, such as the use of an argon atmosphere, hydration chemistry, pH adjustment, low temperature, dispersing MXene in an organic solvent, defect passivation of MXenes, and preparing MXene-polymer composites [43–48]. For example, Zhang et al. successfully developed a tuned microenvironment method to prepare a highly concentrated MXene in organic solvents such as dimethylformamide, dimethylacetamide, and propylene carbonate [45]. Kim et al. successfully prepared stable $Ti_3C_2T_x$ MXene dispersions in nonpolar organic solvents through a simultaneous interfacial chemical grafting reaction and phase transfer method, which exhibits strong oxidation resistance [46]. Considering that most polymers are synthesized in organic solvent systems, as well as practical application and oxidation resistance, the dispersion of MXene in organic solvents can lead to the expansion of the application prospect of MXene composites.

In this study, we successfully synthesized MXene nanosheets with good dispersion in N,N-dimethylacetamide (DMAc) and achieved long-term storage without oxidation by tetrabutylammonium hydroxide (TBAOH) intercalation. In addition, as both DMAc/lithium chloride (DMAc/LiCl) and water/urea/NaOH systems can dissolve microcrystalline cellulose (MCC), for better compatibility with the DMAc-dispersed MXene, DMAc/LiCl was employed as the solvent system for dissolving MCC. This method resulted in improved compatibility of MCC with MXene nanosheets without precipitation. Dielectric nanocomposite films were prepared using cellulose as the matrix and MXene nanosheets (with good dispersibility in DMAc) as inorganic fillers. To the best of our knowledge, this is the first report of MCC–MXene nanocomposite films with improved compatibility between the MXene nanosheets and MCC matrix in a DMAc/LiCl solvent system. This improved compatibility ensures an effectively enhanced dielectric constant, excellent thermal conductivity, and better mechanical properties. More importantly, the proposed strategy not only improves the compatibility between MCC and MXene but also avoids the problem of easy oxidation of MXene in aqueous systems. Consequently, MXene can be preserved for a longer duration, which is essential in building actual composites.

2 Experimental

2.1 Materials

MCC (Avicel PH-101, ~ 50 μm), DMAc, hydrofluoric acid (HF, 48%), and lithium fluoride (powder, 300 mesh) were obtained from Sigma-Aldrich. Lithium chloride (> 98.0%) was supplied by Tokyo Chemical Industry and Ti_3AlC_2 powder (MAX phase, ≥ 99% purity, ~ 400 mesh) was purchased from Jilin 11 Technology Co., Ltd. (China). TBAOH was provided by Alfa Aesar (USA), while hydrochloric acid was supplied by Daejung Chemical Co., Ltd. (Republic of Korea). Double-deionized water was used in all experiments.

2.2 Synthesis of materials

Synthesis of multilayer MXene (M-MXene): M-MXene was obtained by 40% HF aqueous solution etching [49]. First, 40 mL of the HF solution was poured into a Teflon bottle. Subsequently, 2 g of MAX was gradually added to the HF solution over a period of 20 min. This prevents possible overheating during the initial stage of the reaction. After stirring at 35 °C for 24 h, the excess HF was washed off by centrifugation with water. After 9–10 centrifugation cycles, the pH of the supernatant reached 6–7. Finally, the precipitate was collected and dried in a vacuum oven at 60 °C for 24 h. The final powder material was M-MXene. For comparison, we also prepared water-dispersible MXene nanosheets using the MILD method [41]. The details of the preparation process are presented in the Electronic Supplementary Material (ESM).

Synthesis of MXene nanosheet in DMAc: To intercalate M-MXene using TBAOH [45], the organic solvent applied in this study was DMAc. Specifically, the intercalation process was performed by adding 2 g of M-MXene powder to 50 mL of 25% TBAOH solution with stirring at room temperature for 24 h. Subsequently, excess TBAOH was removed by washing with

ethanol, after which all precipitates were collected. Then, to completely disperse the precipitates, approximately 70 mL of the DMAc solution was poured into a centrifuge tube and shaken thoroughly (Fig. 1(a)).

Preparation of MCC–MXene nanocomposite films: A total of 1.6 g of LiCl was dissolved in 12.5 mL of DMAc to prepare a LiCl/DMAc solvent. To prepare LiCl/DMAc solutions with different MXene contents, different volumes of DMAc/MXene solutions were added to LiCl/DMAc while controlling the total volume of the solution at 12.5 mL. In addition, 0.8 g of MCC was dispersed in another bottle containing 6.5 mL of DMAc. The mixture was then stirred at room temperature for 24 h. Afterward, the two dispersions were mixed and stirred well for 24 h. Subsequently, the suspensions were cast evenly onto the surface of a glass plate at room temperature. The plates were immediately transferred to a chamber with a constant temperature of 35 °C and relative humidity (RH) of 85% for 24 h. The resultant hydrogel membranes were thoroughly washed with deionized water by soaking to completely remove the residual small molecules. Finally, the MCC–MXene composite hydrogel membranes were dried in a constant temperature and humidity chamber at 25 °C and 65% RH for 24 h to remove any residual solvent. In this way, MCC–MXene nanocomposite films containing 0 wt.%, 3 wt.%, 5 wt.%, 10 wt.%, 20 wt.%, and 30 wt.% of MXene nanosheets were obtained. The synthesis steps are illustrated in Fig. 1(h).

2.3 Characterization

The functional groups of the nanocomposite films were characterized by Fourier transform infrared (FTIR, JASCO FTIR-4100) spectroscopy in the range of 500–4,000 cm^{-1}. The size distribution of MXene was measured using dynamic light scattering (DLS; Zetasizer NANO-S90, Malvern). Thermogravimetric analysis (TGA) was performed using Perkin–Elmer Pyris Diamond TG at a heating rate of 5 °C·min^{-1} under a N_2 atmosphere. X-ray photoelectron spectroscopy (XPS) was carried out on a Theta Probe AR-XPS system (Thermo Fisher Scientific, UK). The crystal structures were verified using X-ray diffraction (XRD, Bruker AXS) in the 2θ range of 5°–80°. The morphology of MXene was characterized by transmission electron microscopy (TEM, JEOL 2011) at an acceleration voltage of 200 kV. The surface and cross-sectional morphologies and elemental mapping of the samples were observed by field emission scanning electron microscopy (FESEM, ZEISS SUPRA 25 VP) combined with energy-dispersive X-ray spectroscopy (EDX). To obtain relatively reliable cross-sectional information, the MCC–MXene nanocomposite films were immersed in liquid nitrogen and then broken. The topography and roughness of the samples were examined using atomic force microscopy (AFM, Park NX10). The absorbance of MXene nanosheets was measured using a ultraviolet–visible (UV–vis) spectrometer (Optizen 3220UV). The dielectric properties of the MCC–MXene nanocomposite films were obtained using a broad-frequency dielectric spectrometer (Concept 80, Novocontrol, Germany) at room temperature in the frequency range of 10^0–10^7 Hz. The coefficient of thermal expansion (CTE) of the MCC–MXene nanocomposite films was measured using a thermomechanical analyzer (TMA, Q400, TA Instruments, USA)) in the temperature range of 30–140 °C at a heating rate of 5 °C·min^{-1}. A universal testing machine (LRX PLUS, Lloyd Instrument, UK) was used to test the mechanical properties of the MCC–MXene nanocomposite films at a strain rate of 3 mm·min^{-1}, in accordance with ASTM D882. The sample length and width were 25 and 5 mm, respectively. Each sample was tested five times to evaluate its mechanical properties. The water uptake was calculated by measuring the change in weight of the samples after exposure for 24 h in a constant temperature and humidity chamber at 25 °C with an RH range of 65%–90%. The thermal diffusivity of the nanocomposite film was measured by the laser flash method using LFA 467 (NETZSCH, Germany) at 30 °C. The thermal conductivity was then calculated as $K = \alpha C_p \rho$, where α and ρ are the thermal diffusivity and density of the nanocomposite film, respectively; ρ is the density calculated using a weighing method; and C_p is the specific heat capacity measured using a differential scanning calorimeter (Q100 TA Instruments, New Castle, DE,

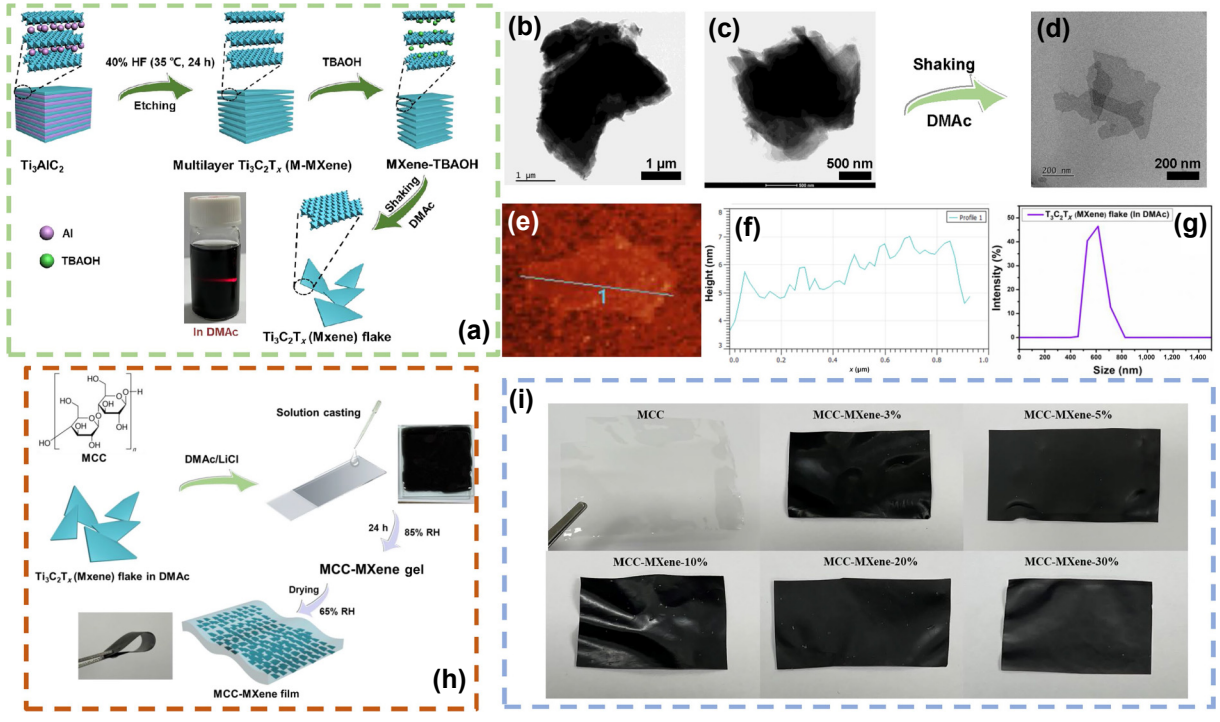

Figure 1 (a) Schematic of the preparation of MXene nanosheets. (b) TEM image of M-MXene. (c) TEM image of MXene–TBAOH. (d) TEM image of MXene nanosheets. (e) AFM image of MXene nanosheets. (f) Height profiles of MXene nanosheets. (g) Particle size distribution of MXene nanosheets dispersed in DMAc. (h) Schematic of the preparation of MCC–MXene nanocomposite films. (i) Photographs of MCC and MCC–MXene nanocomposite films.

USA). The contact angle of the nanocomposite film was measured using a contact angle analyzer (SEO Pheonix 300). The bacteriostatic performance of the samples was evaluated using the standard colony counting method. The microbe was activated in a Luria-Bertani (LB) medium at 30 °C. The microbial suspension was diluted and adjusted to 1 mL. The nanocomposite films (cut into 1 cm × 1 cm) and MXene nanosheet dispersions were immersed in the diluted suspension and incubated at 30 °C with shaking for 5 h. Then, 5 μL of the suspensions was spread onto the surface of the LB solid medium. The solid medium was cultured at 30 °C for 10 h, and the viable numbers of microbial colonies were counted by visual observation. The cell suspension without samples was used as the control.

3 Results and discussion

3.1 Microstructure of MXene nanosheets

The MAX phase (Ti_3AlC_2 powder, Figs. S1(a) and S1(c) in the ESM) was selectively etched into M-MXene (Figs. S1(b) and S1(d) in the ESM) using 40% HF. After selective etching, an accordion-like multilayered morphology of the M-MXene was successfully obtained. The TEM images of M-MXene, MXene–TBAOH, and exfoliated MXene are illustrated in Figs. 1(b)–1(d). Semitransparent flakes are clearly observed (Fig. 1(d)), indicating the successful exfoliation of MXene–TBAOH into MXene nanosheets by shaking in the DMAc solution. MXene nanosheets have lateral diameters ranging from 400 nm to 1.2 μm, as shown in Fig. S2 in the ESM. AFM analysis shows that the average thickness of MXene is approximately 2.5 nm (Figs. 1(e) and 1(f)), confirming the nanosheet structure of MXene. The size of the MXene nanosheets was determined by DLS analysis. The average size of the main peak with a large number of nanosheets is 615 nm, as shown in Fig. 1(g). The Tyndall effect reveals that the MXene nanosheets have good dispersity in DMAc (inset of Fig. 1(a)). Figure 1(i) displays photographs of the as-prepared pure MCC and MCC–MXene nanocomposite films. The structural information of Ti_3AlC_2, M-MXene, and MXene–TBAOH was obtained using XRD, as depicted in Figs. 2(a) and 2(b). After the etching process, the characteristic (104) peak at 2θ = 39° that belongs to Ti_3AlC_2 MAX powder diminishes, and the (002) peak exhibits a shift to a lower 2θ angle from 9.77° (d = 0.904 nm) to 8.87° (d = 0.996 nm) (Fig. 2(b)). After insertion of the TBAOH, the (002) peak of the M-MXene powder shifts significantly from a 2θ angle of 8.87° (d = 0.996 nm) to 5.69° (d = 1.551 nm), indicating that TBAOH is successfully intercalated into M-MXene [45].

The FTIR spectra of M-MXene and MXene–TBAOH are illustrated in Fig. 2(c). M-MXene has four typical peaks at 3,427, 1,632, 1,206, and 545 cm^{-1}, corresponding to the stretching vibrations of the –OH, C=O, C–F, and Ti–O bonds, respectively. The corresponding characteristic diffraction peaks are also observed in the MXene–TBAOH. Meanwhile, after intercalation of TBAOH into MXene, the characteristic peaks of MXene–TBAOH become slightly weaker than those of M-MXene. This result also indicates that TBAOH is successfully intercalated into M-MXene [50, 51].

The TGA curves of Ti_3AlC_2, M-MXene, and MXene–TBAOH are presented in Fig. 2(d). Ti_3AlC_2 exhibits a high thermal stability without any weight loss at 600 °C. Instead, there is a slight increase in weight, probably because the N_2 used contains a trace amount of oxygen, and the aluminum in Ti_3AlC_2 is slightly oxidized at high temperature [52]. The weight loss of M-MXene is 6.8 wt.%, which is attributed to the introduction of –F, –OH, and –O groups after etching. After intercalation of TBAOH into M-MXene, the weight loss of the MXene–TBAOH increases to 16.2 wt.%. The TGA results further indicate the successful etching of Ti_3AlC_2 and the intercalation of TBAOH into MXene.

The surface electronic states and surface compositions of the M-MXene and MXene–TBAOH powders were analyzed using XPS (Figs. 2(e) and 2(f) and Fig. S3 in the ESM). The C1s XPS spectrum of M-MXene (Fig. S3(b) in the ESM) shows three peaks at binding energies of 281.4, 284.5, and 288.4 eV, which are assigned to the C–Ti, C–C, and C–O bonds, respectively. The initial 281.4 eV peak corresponding to C–Ti (for M-MXene) is changed to 281.1 eV, which corresponds to the C–Ti bond after intercalation with TBAOH (Fig. S3(e) in the ESM). This result suggests that the chemical environment of Ti atoms on the surface of M-MXene may have changed [45]. The O1s XPS spectrum (Figs. 2(e) and 2(f)) shows four peaks at binding energies of 529.5,

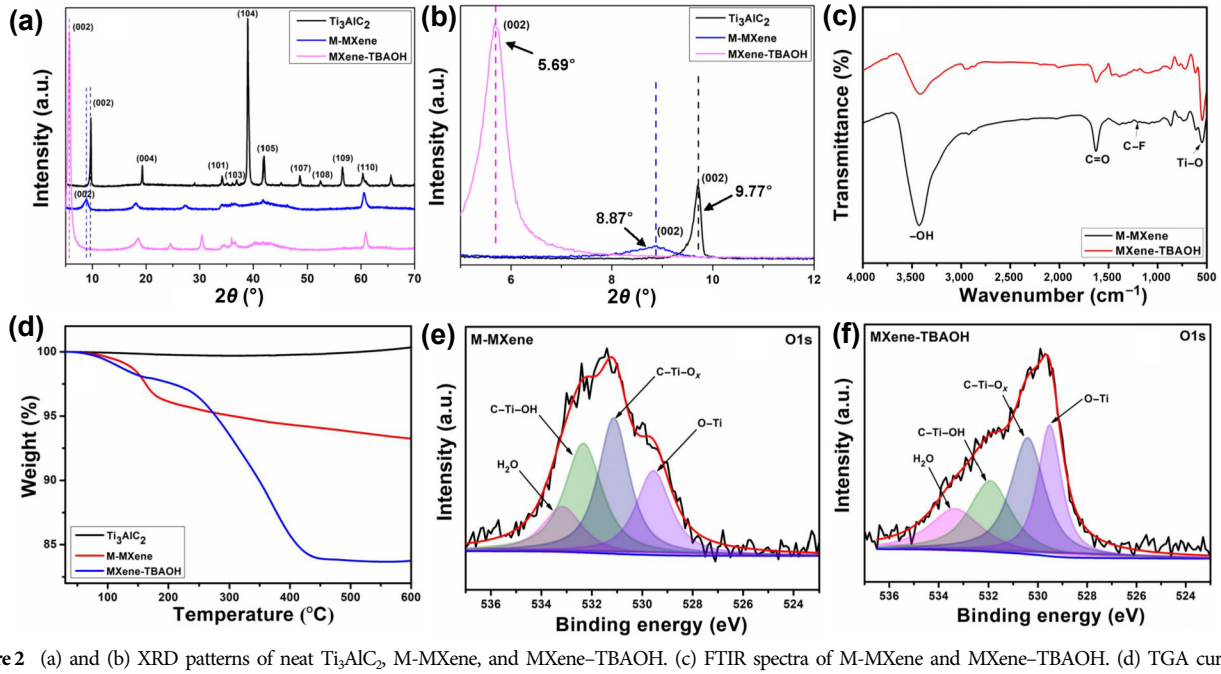

Figure 2 (a) and (b) XRD patterns of neat Ti_3AlC_2, M-MXene, and MXene–TBAOH. (c) FTIR spectra of M-MXene and MXene–TBAOH. (d) TGA curves of Ti_3AlC_2, M-MXene, and MXene–TBAOH. (e) High-resolution XPS spectra of O1s for M-MXene. (f) High-resolution XPS spectra of O1s for MXene–TBAOH.

531.1, 532.3, and 533.2 eV, which are attributed to the adsorption of O species: O–Ti, C–Ti–O_x, C–Ti–OH, and H_2O, respectively. It can be seen that the content of C–Ti–OH in MXene–TBAOH is reduced compared with that in M-MXene. Therefore, based on the discussion of the above XPS results, the intercalation of TBAOH may plausibly replace some of the –OH on the surface groups of M-MXene. In addition, high-resolution spectra in the Ti2p region for M-MXene and MXene–TBAOH are displayed in Figs. S3(c) and S3(f) in the ESM. In Fig. S3(c) in the ESM, the Ti2p spectrum of the M-MXene sample shows four dominant peaks at 454.5, 455.3, 456.1, and 457.2 eV, corresponding to the Ti–C, Ti(II), Ti(III), and Ti–O bonds, respectively. Figure S3(f) in the ESM illustrates the Ti2p spectrum of the MXene–TBAOH sample. After intercalation with TBAOH, the four dominant peaks corresponding to Ti–C, Ti(II), Ti(III), and Ti–O bonds change to 454.7, 455.5, 456.5, and 458.5 eV, respectively [53, 54]. This result further proves the change in the surface environment of MXene, which may provide better dispersion of MXene in DMAc.

3.2 Microstructure and thermomechanical and mechanical properties of MCC–MXene nanocomposite films

Figures 3(a)–3(c) depict the TEM images of the MXene, MCC, and MCC–MXene suspensions, respectively. After mixing the MCC and MXene, the MCC adheres to the MXene nanosheets, which is attributed to the hydrogen bonding forces between the hydroxyl groups on the MCC and the oxygen-containing groups on the surface of MXene. The intimate integration and uniform distribution of MXene nanosheets may endow the nanocomposite films prepared from this solution with higher mechanical strength. In addition, complete dispersion of MXene filler facilitates uniform packing of the MCC–MXene nanocomposite films, leading to better dielectric properties. The cross-section morphologies of the pure MCC and MCC–MXene nanocomposite films with various filler contents ranging from 3 wt.% to 30 wt.% were investigated using FESEM images (Figs. 3(d)–3(i)). The pure MCC exhibits a dense cross-section without obvious cracks or voids, indicating the successful synthesis and good quality of pure MCC films. Moreover, the morphological changes induced by MXene fillers on the MCC are very clear. Compared with that of the pristine MCC films, the fractured cross-section of the MCC–MXene nanocomposite films clearly presents a more layered structure. Meanwhile, the SEM images of MCC–MXene nanocomposite films show that MXene nanosheets are uniformly distributed in the MCC substrate without congregation. Additionally, the MXene nanosheets are well aligned, with their sheet plane parallel to the surface of the nanocomposite films. This result can be attributed to the strong interaction between the MCC and MXene nanosheets. Low-resolution cross-sectional SEM images of the as-synthesized pristine MCC and MCC–MXene nanocomposite films are depicted in Fig. S4 in the ESM, which indicates typical film structures. Moreover, elemental mapping was performed to study the dispersibility of the components in the MCC–MXene nanocomposite films. The results demonstrate the coexistence of C and O in neat MCC (Fig. S5 in the ESM). In the MCC–MXene-20% nanocomposite films (Fig. 4(d)), Ti appears and its content is 14.3%. The elemental mapping images show a homogeneous distribution of Ti and C in the nanocomposite films, indicating good compatibility and uniform distribution of MCC and MXene. Meanwhile, the amount of Ti increases from 3.0 wt.% to 16.5 wt.% owing to the different contents of MXene nanosheets doped into the MCC matrix (Figs. S5–S10 in the ESM).

According to the XPS spectra of MXene–TBAOH and MCC–MXene-30% (Figs. 3(j) and 3(l)), the C:Ti and O:Ti ratios of MXene–TBAOH are 5.97 and 1.64, respectively, while those of MCC–MXene-30% are 31.28 and 18.66, respectively. Therefore, the C:Ti and O:Ti ratios of MCC–MXene-30% are higher than those of MXene–TBAOH. The experimental results indicate that

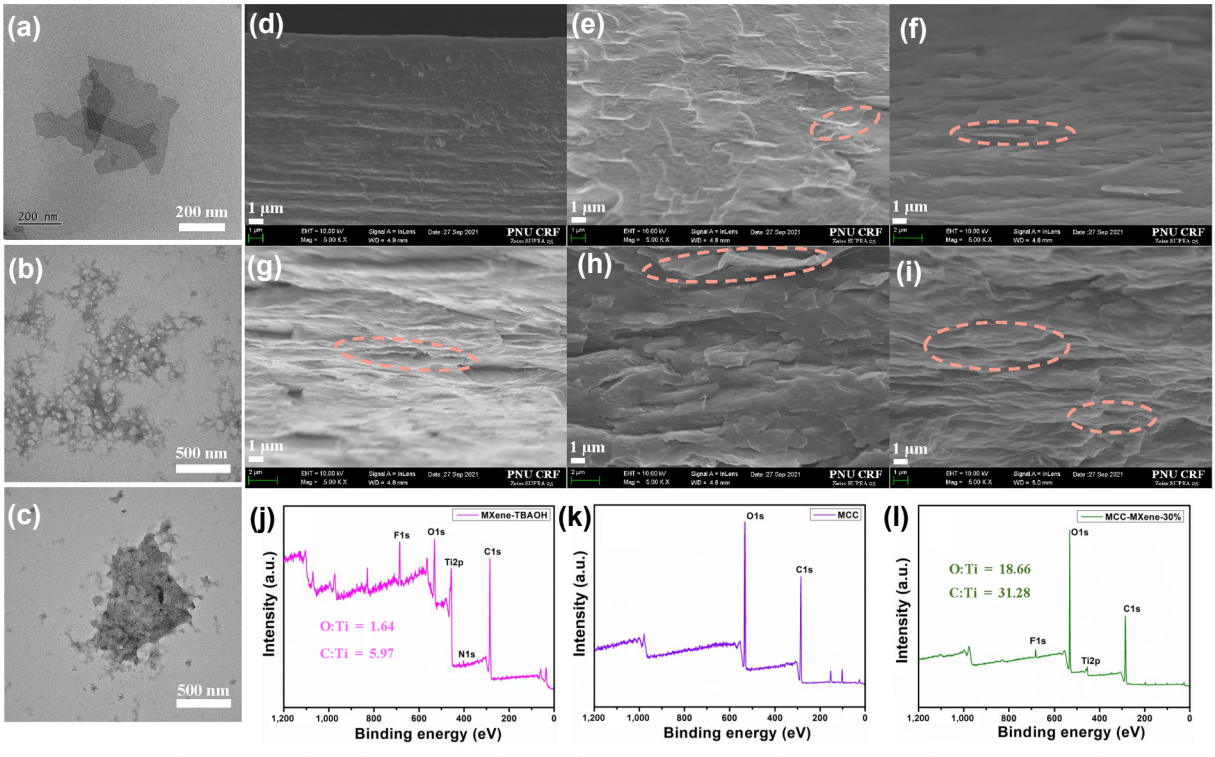

Figure 3 (a) TEM image of MXene nanosheets. (b) TEM image of MCC solution. (c) TEM image of MCC–MXene solution. Cross-sectional SEM images of (d) pristine MCC, (e) MCC–MXene-3%, (f) MCC–MXene-5%, (g) MCC–MXene-10%, (h) MCC–MXene-20%, and (i) MCC–MXene-30% nanocomposite films, where the orange circles with dotted lines represent layered structures of MXene nanosheets. XPS wide-scan spectra of (j) MXene–TBAOH, (k) MCC, and (l) MCC–MXene-30% nanocomposite films.

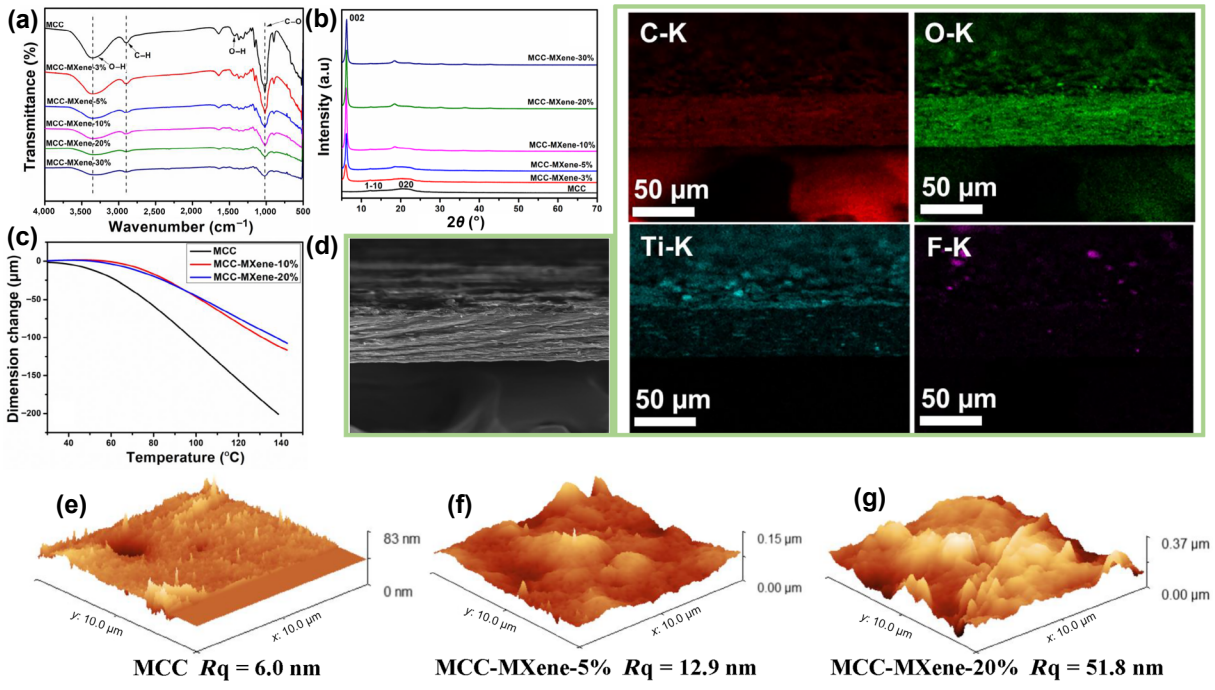

Figure 4 (a) FTIR spectra of neat MCC and MCC–MXene nanocomposite films with different MXene contents. (b) XRD patterns of neat MCC and MCC–MXene nanocomposite films with different MXene contents. (c) TMA curves of neat MCC film, MCC–MXene-10%, and MCC–MXene-20% nanocomposite films. (d) SEM-EDX mapping micrographs of MCC–MXene-20%. AFM images of 10 μm × 10 μm surfaces of (e) neat MCC film, (f) MCC–MXene-5%, and (g) MCC–MXene-20% nanocomposite films.

the MCC and MXene nanosheets are successfully introduced into the as-prepared nanocomposite films [55].

The FTIR spectra of the pure MCC and MCC–MXene nanocomposite films are depicted in Fig. 4(a). The cellulose characteristic absorption bands at 3,353 (O–H stretching), 2,903 (C–H stretching), 1,429 (–OH bending), and 1,020 cm^{-1} (C–O stretching) are observed in the FTIR spectra of the MCC–MXene nanocomposite films. With the increase in MXene content, the characteristic peak intensity of cellulose weakens, which also proves the successful synthesis of nanocomposites with different MXene contents [51]. The XRD patterns of the MCC and MCC–MXene nanocomposite films with different MXene contents are shown in Fig. 4(b) and Fig. S11 in the ESM. The diffraction peaks at 2θ angle = 12.3° and 20.8° respectively correspond to the ($1\bar{1}0$) and (020) crystal planes of the cellulose II crystalline structure [56, 57]. When the MXene content is increased from 3 wt.% to 30 wt.% in the nanocomposite film, the two representative peaks of the MCC become weaker. Furthermore, to demonstrate the successful intercalation of MCC into MXene nanosheets, we analyzed the (002) characteristic peaks of different samples. However, because of the intercalation through TBAOH, the 2θ angle of the (002) peak of MXene–TBAOH is smaller than those of all MCC–MXene nanocomposite films. This may be due to the restacking of MXene during drying after intercalation and exfoliation, and the intercalation effect of the MCC may not be as significant as that of TBAOH. Therefore, we further compared the as-synthesized nanocomposite films with MXene nanosheets synthesized using the MILD method. The characteristic (002) peak shifts from 2θ = 6.51° (MXene-MILD) to 6.04° (MCC–MXene-3%), 6.19° (MCC–MXene-5%), 6.15° (MCC–MXene-10%), 6.20° (MCC–MXene-20%), and 6.25° (MCC–MXene-30%), implying that the *d*-spacing of the MCC–MXene nanocomposite film is larger than that of MXene (LiF + HCl, MILD). Meanwhile, with the increase in MXene content, the *d*-spacing decreases owing to the decrease in the relative amount of MCC. The change in the *d*-spacing strongly proves the successful intercalation of MCC into the MXene nanosheets [51].

To further demonstrate the uniform distribution of MXene nanosheets in the MCC matrix, the microstructures of the nanocomposite films were analyzed using AFM. The surface topography and roughness of the MCC–MXene nanocomposite films were investigated using a scan area of 10 μm × 10 μm, and the results are presented in Figs. 4(e)–4(g) and Fig. S12 in the ESM. The surface of the MCC–MXene nanocomposite films is smooth, and the root-mean-square (*Rq*) roughness values of the nanocomposite films containing 0 wt.%, 5 wt.%, 10 wt.%, 20 wt.%, and 30 wt.% MXene are 6.0, 12.9, 7.5, 51.8, and 30.9 nm, respectively. With the introduction of MXene, the surface roughness tends to increase. The inconsistent increasing trend in the roughness with increasing MXene content may be because different surface regions of the nanocomposite films were selected during the test process and measurement errors might have incurred. However, even the 20% and 30% MXene loadings did not drastically increase the surface roughness of the nanocomposite films, which remained in the nanoscale range (less than 60 nm), although the MXene size we used was approximately 400 nm to 1.2 μm. This can be attributed to the unique sheet structure of MXene. The acceptable surface roughness of the nanocomposite films can safeguard their potential application in dielectric devices as it can minimize various performance perturbations that can be caused by surface defects.

High dimensional stability is an important feature of polymer-based nanocomposites for their potential application in flexible electronic devices. The thermomechanical properties of the MCC–MXene nanocomposite films were measured using a TMA. The incorporation of MXene remarkably decreased the CTE of MCC–MXene nanocomposite films. The results are shown in Fig. 4(c) and summarized in Table S1 in the ESM. The CTE of the MCC–MXene nanocomposite films decreases with increasing MXene nanosheet loading. The CTE values decrease from 15.0 $ppm{\cdot}K^{-1}$ for pristine MCC to 8.2 $ppm{\cdot}K^{-1}$ for the MCC–MXene-20% nanocomposite films over the temperature range of 70–140 °C. The addition of 2D MXene nanosheets is believed to enhance the chain orientation of MCC, resulting in a

lower CTE. In addition, the homogeneous dispersion of MXene nanosheets in the MCC matrix can decrease the free volume in the matrix and consequently reduce the CTE of the nanocomposite films [58, 59].

Tensile testing was conducted to evaluate the mechanical properties of the resulting MCC–MXene nanocomposite films with various MXene contents. The stress–strain curves and data are shown in Figs. 5(a)–5(d) and Table S2 in the ESM. The pure MCC film exhibits a tensile strength, Young's modulus, and elongation at break of 119.2 ± 7 MPa, 3654.7 ± 445 MPa, and 7.6% ± 4%, respectively. After compounding with MXene, the mechanical properties of the nanocomposite films considerably improved. The tensile strengths of MCC–MXene-20% and MCC–MXene-30% reach 183.9 ± 9 and 188.8 ± 8 MPa, respectively, which are almost 1.5 and 1.6 times higher than that of pristine MCC. Moreover, the Young's moduli of the MCC–MXene-20% and MCC–MXene-30% nanocomposite films are higher than that of pure MCC (Fig. 5(c)). The MCC–MXene-30% nanocomposite film exhibits an elongation at break of 14.3% ± 2%, which is almost 1.9 times higher than that of the pure MCC film (Fig. 5(d)). The improvement in mechanical properties is attributed to the mechanical entanglement and interfacial interaction (hydrogen bonding) between the 2D MXene nanosheets and the MCC network. The enhancement in tensile strength by mechanical entanglement can be due to the good dispersion of both MXene sheets and MCC in the nanocomposites, owing to their excellent dispersibility and solubility in the DMAc/LiCl system. As a result, flexible MCC is embedded into the spatial gaps in the MXene nanoflakes during drying-induced self-assembly, leading to a densely packed structure with few vacancies. Figure 5(e) displays photographs of the bent states of MCC and MCC–MXene nanocomposite films. Figure 5(g) illustrates the possible mechanical entanglement states of the MCC–MXene nanocomposite film. The 2D MXene nanosheets act as "bricks" and provide the framework for the nanocomposite films, while the one-dimensional MCC acts as a flexible "cement" connecting the MXene nanosheets [60]. Therefore, through the synergistic effect of MCC and MXene, a strong layer-by-layer structure is formed, leading to tension transfer and energy dissipation during the stretching process, which is beneficial for improving the mechanical properties. In addition, the strong hydrogen bonding interaction between the MXene sheets and MCC fibrils significantly enhances the load transfer in the nanocomposite film, which greatly contributes to the improvement in the mechanical properties (Fig. 5(g)). We demonstrated the formation of hydrogen bonds using high-resolution FTIR spectroscopy (Fig. 5(f) and Fig. S13 in the ESM). Compared with the MCC film, the O–H peaks of MCC–MXene-10%, MCC–MXene-20%, and MCC–MXene-30% films are redshifted to 3,450, 3,329, and 3,327 cm^{-1}, respectively, indicating the formation of hydrogen bonds between the MXene and MCC molecules [33, 61]. Figure 5(g) shows how the hydroxyl groups on the cellulose molecular chains form hydrogen bonds with the functional groups on MXene. The hydrogen bonding between MXene and MCC leads to a robust structure. More importantly, although the use of the DMAc/LiCl solvent system results in better dispersion and compatibility between MCC and MXene, the hydrogen bonding interaction further promotes homogeneous dispersion of MXene in the MCC solution. Consequently, we believe that the hydrogen bonding between the cellulose substrate and MXene nanosheets and the good dispersion and compatibility of MXene and MCC contribute significantly to achieving homogeneous nanocomposite films with desirable mechanical performance.

3.3 Dielectric properties of MCC–MXene nanocomposite films

The dielectric constant and dielectric loss of MCC–MXene films

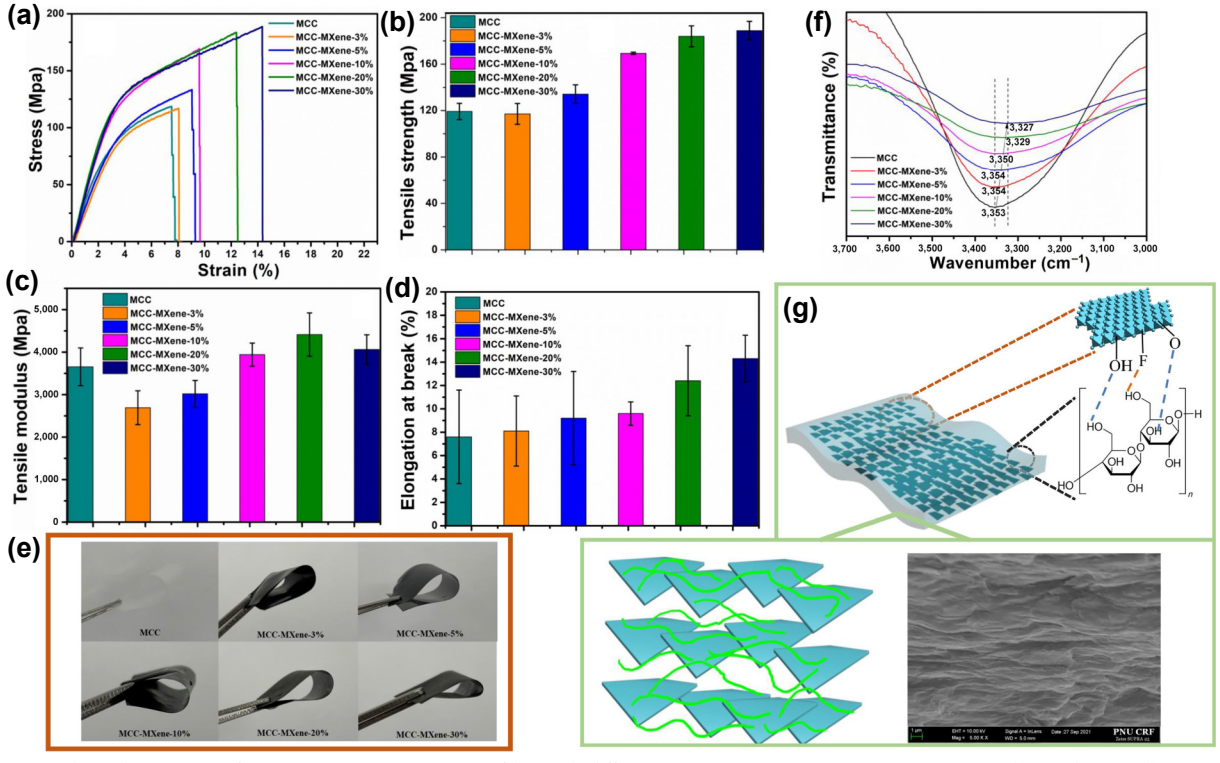

Figure 5 Mechanical properties of MCC–MXene nanocomposite films with different MXene contents: (a) stress–strain curves, (b) tensile strength, (c) Young's modulus, and (d) elongation at break. (e) Photographs of the bent state of MCC and MCC–MXene nanocomposite films. (f) High-resolution FTIR spectra of neat MCC and MCC–MXene nanocomposite films with different MXene contents. (g) Schematic of mechanical entanglement and hydrogen bonds between MXene nanosheets and MCC.

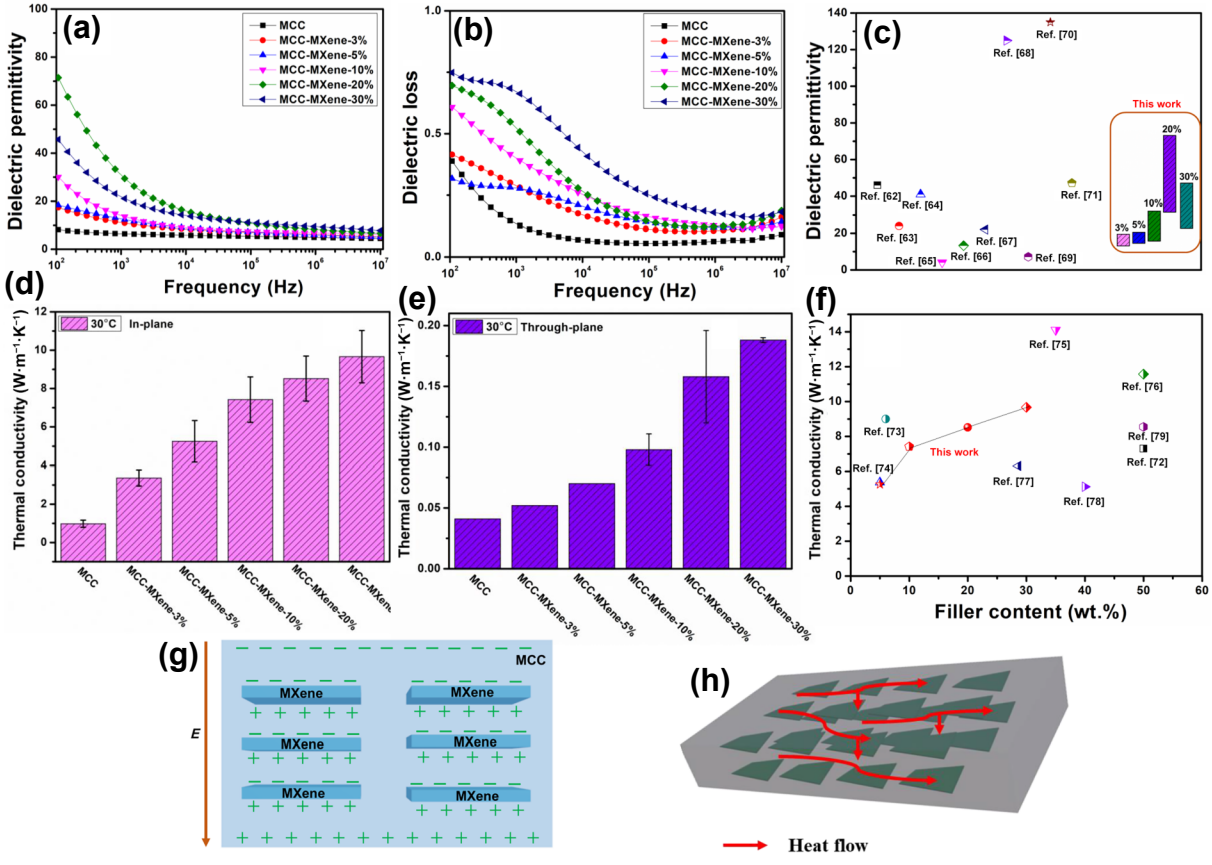

Figure 6 (a) Permittivity of the MCC–MXene nanocomposite films with different weight fractions. (b) Dielectric loss of the MCC–MXene nanocomposite films with different weight fractions. (c) Comparison of the permittivity of MCC–MXene n nanocomposite films with those of other reported cellulose-based nanocomposites or composites containing MXene fillers [62–71]. (d) In-plane thermal conductivity of MCC–MXene nanocomposite films with various MXene contents. (e) Through-plane thermal conductivity of MCC–MXene nanocomposite films with various MXene contents. (f) Comparison of the in-plane thermal conductivity of MCC–MXene nanocomposite films with those of other reported cellulose-based nanocomposites or composites containing MXene fillers [72–79]. (g) Possible interfacial polarization mechanisms of MCC–MXene nanocomposite films under an external electric field (*E*). (h) Proposed model of MCC–MXene for thermal conduction.

with different amounts of MXene nanosheets are presented in Figs. 6(a) and 6(b). As shown, the dielectric permittivity of the MCC–MXene nanocomposites initially increases with increasing MXene filler concentration. A dielectric constant of > 70 (10^2 Hz) is obtained for a nanocomposite with 20 wt.% MXene. The enhanced dielectric constant with increasing MXene content can be attributed to two important phenomena, namely, microscopic dipole formation (the dielectric performance difference between MXene and MCC) and microcapacitor network formation, both of which lead to interfacial polarization of the nanocomposite film at the interface between the conducting MXene and host MCC polymer [29, 36]. The possible interfacial polarization mechanisms of the MCC–MXene nanocomposite films are illustrated in Fig. 6(g). In the microscopic dipole model, generally predominant at lower levels of MXene fillers, when an electric field (E) is applied to the film, charges accumulate at the interface between the MXene nanosheets and MCC matrix, forming corresponding microscopic dipoles. In the microcapacitor network model, when the content of MXene nanosheets reaches a certain amount, microcapacitors are created when adjacent MXene nanosheets become close such that only a very thin MCC dielectric layer is left between them. Each microcapacitor contributes to the capacitance of the entire nanocomposite film microcapacitor network, which increases the dielectric constant near the permeation limit [29]. A further increase in the amount of MXene filler decreases the dielectric constant, which may be because the MCC–MXene nanocomposite has reached the percolation limit (φ_c). The decrease in permittivity may be due to the increased connectivity between MXene sheets, leading to an increase in leakage current at higher MXene filler contents, which in turn causes a transition of MCC–MXene nanocomposite film from non-ohmic to ohmic conduction [36]. Figure 6(b) shows that the dielectric loss also increases with increasing content of MXene nanosheets. It is worth noting that the dielectric loss of the MCC–MXene nanocomposite film only increases approximately 1.8 times (from 0.39 to 0.70) up to 20 wt.% MXene filler, while the permittivity increases approximately 8.7 times (from 8.2 to 71.4) over the same composition range.

Two factors primarily cause the improvement in the dielectric constant of MCC–MXene nanocomposite materials. The first factor is the excellent electrical conductivity of MXene nanosheets, which increases the electrical conductivity difference between the MXene filler and insulating MCC matrix, thereby enhancing the interfacial polarization through the microscopic dipole model. The second factor is the dispersion state of MXene inside the MCC matrix, which in our case is excellent and is responsible for the formation of the microcapacitor (uniform and efficient mutual stacking of MCC and MXene owing to the use of the DMAc/LiCl solvent system). In addition to these two major factors, another possible reason is hydrogen bonding. The formation of hydrogen bonds between MXene and MCC was confirmed by FTIR spectroscopy. Previous studies have suggested that hydrogen bonds may also form dipoles when an electric field is applied [29].

The previously reported dielectric constants of cellulose-based composites and nanocomposites containing MXene fillers are summarized and compared with those of MCC–MXene

nanocomposite films (Fig. 6(c) and Table S3 in the ESM). As indicated, the dielectric constants of our synthesized MCC–MXene nanocomposite films are comparable to those of cellulose-based composites or nanocomposite materials with MXene as fillers. In addition, the dielectric loss of the MCC–MXene nanocomposite film, which is an important parameter that must be evaluated, is not particularly low, because from our data, the dielectric loss of pure MCC is already approximately 0.39 (10^2 Hz). However, it does not increase sharply with an increase in MXene filler, and it increases to 0.7 (10^2 Hz) when the MXene content is 20%. In general, conductive materials tend to cause a considerable increase in dielectric loss at high filler contents owing to the surge in the formation of conductive path networks. For example, with increasing rGO concentration in cyanoethyl cellulose, the dielectric loss increases from 0.08 to 0.7 (with 6.8% rGO), and then to 4.1 (with 9.7% rGO), as reported by Wang et al. [68]. The better control of dielectric loss by MCC–MXene may be attributed to the good compatibility between MCC and MXene owing to the use of the DMAc/LiCl system. MXene can be uniformly dispersed in the MCC matrix and stacked layer by layer in the thickness direction (electric field direction) of the film. The inclusion of MCC between layers of MXene prevents substantial conductive connections in the direction of the electric field. More importantly, in terms of stability, owing to the use of the DMAc/LiCl system, the dielectric properties of the nanocomposite films prepared by the MCC–MXene mixed solution after long-term storage are not significantly compromised, which will be discussed in more detail in Section 3.7.

3.4 Thermal conductivity of MCC–MXene nanocomposite films

For portable electronic products, the electronic components therein generate a large amount of thermal energy, which adversely affects their function and service life; thus, thermally controllable dielectric materials are necessary for such electronic products. The thermal conductivities of the MCC–MXene nanocomposite films were characterized using LFA 467 NanoFlash. Figures 6(d) and 6(e) display the in-plane and through-plane thermal conductivities of the nanocomposite films with different MXene contents. It can be observed that the in-plane thermal conductivity of the MCC–MXene nanocomposite films can be effectively improved by increasing the MXene loading. The in-plane thermal conductivity of the pure MCC film at 30 °C is approximately 0.976 $W \cdot m^{-1} \cdot K^{-1}$. When the MXene filler content is 3 wt.%, the in-plane thermal conductivity increases from 0.976 to 3.363 $W \cdot m^{-1} \cdot K^{-1}$. As the MXene content is further increased to 20 wt.% and 30 wt.%, the thermal conductivity increases to 8.523 and 9.668 $W \cdot m^{-1} \cdot K^{-1}$, respectively. On the other hand, it can be noted that the through-plane thermal conductivity is low for all samples with different amounts of MXene fillers. The through-plane thermal conductivity increases from 0.041 $W \cdot m^{-1} \cdot K^{-1}$ for the pure MCC film to 0.188 $W \cdot m^{-1} \cdot K^{-1}$ for the MCC–MXene-30% film. The in-plane thermal conductivity is significantly higher than that of the through-plane. From this information, we can infer that the thermal conductivity of the MCC–MXene nanocomposite film is strongly anisotropic. The thermal conductivity anisotropy is believed to be caused by the layer-by-layer structure consisting of the MCC matrix and aligned MXene nanosheets. The cross-sectional SEM images of the MCC–MXene films in Fig. 3(i) show that the 2D MXene nanosheets are aligned in the planar direction and the layered structure is perfectly retained. Because DMAc/LiCl is used as the mixed solvent system for cellulose and MXene (stably dispersed in DMAc), a uniform distribution of MCC between the MXene nanosheets can be clearly observed. A continuous thermal conduction network in the in-plane direction is provided by the MXene layer in the MCC–MXene nanocomposite film. Overlapping MXene nanosheets in the MCC–MXene nanocomposite films can effectively reduce the interfacial thermal resistance between fillers, providing a means for phonon conduction [35]. Thus, the heat flux can be efficiently dissipated along the continuous MXene nanosheet layer, which greatly enhances the in-plane thermal conductivity in the MCC–MXene film. However, the MCC between the MXene layers strongly hinders thermal transportation along the through-plane direction. Figure 6(h) shows a possible thermal conduction model for the nanocomposite films. In addition, it is worth noting that the in-plane thermal conductivities of the MCC–MXene nanocomposite films are comparable to those of other cellulose-based nanocomposites or composites containing MXene fillers, which meet the requirements of thermal management devices, as depicted in Fig. 6(f) and Table S4 in the ESM. In summary, the excellent in-plane thermal conductivity of the MCC–MXene nanocomposite films makes them suitable for thermal management applications and may effectively improve the service life of MCC–MXene dielectric materials.

3.5 Thermal stability and fire safety

Excellent fire safety is critical in the field of electronic materials. To evaluate their flame resistance, the MCC–MXene nanocomposite films were exposed to a lighter flame. Because the pure MCC film contains numerous unstable oxygen-containing groups, such as hydroxyl groups, once the MCC is ignited, it burns violently and only takes 5 s to burn completely with almost no residue. Comparatively, the MCC–MXene-30% is more difficult to ignite. The flame is smaller and the sample shrinkage is not obvious after burning (Fig. 7(a)). The physical barrier and carbonization effects of MXene nanosheets may play an important role in improving the flame retardancy of MCC–MXene nanocomposite films. MXene nanosheets are oxidized to TiO_2 at a high flame temperature, thereby forming a TiO_2 layer that can act as a physical barrier to prevent heat transfer in the nanocomposite film, which further improves the flame retardant performance of the MCC–MXene nanocomposite films [80, 81]. The excellent thermal stability of MCC–MXene was also confirmed by TGA. The TGA and differential thermal gravity (DTG) curves are depicted in Figs. 7(b) and 7(c). Figure 7(b) shows that the pure MCC and MCC–MXene nanocomposite films exhibit two-step weight losses. After introducing the MXene nanosheets, the MCC–MXene nanocomposite film still maintains a thermal decomposition curve similar to that of the MCC. The thermal decomposition temperature (T_d) at 5% weight loss of MCC–MXene increases when the MXene content increases from 0% to 5%; however, it shows a decreasing trend when the MXene content exceeds 10%. It is believed that the easily decomposed hydroxyl groups in MXene (when the MXene content is high) may have accelerated the degradation of MCC-MXene, leading to the decline in the thermal stability of the MCC-MXene at low temperatures. However, as shown in the DTG curves (Fig. 7(c)), compared with that of the MCC film, the maximum weight loss rate of the MCC–MXene nanocomposite film has a significant decrease trend. This may be due to the "barrier effect" of MXene nanosheets, which hinders the diffusion of volatile compounds. The thermal conductivity of MXene nanosheets endows the nanocomposite film with the ability to dissipate heat faster. In addition, the MCC–MXene-30% film shows a relatively higher char yield (from 27% for MCC to 45%), indicating that the introduction of MXene into the nanocomposite film can enhance thermal stability. Moreover, the oxide of MXene can further act as

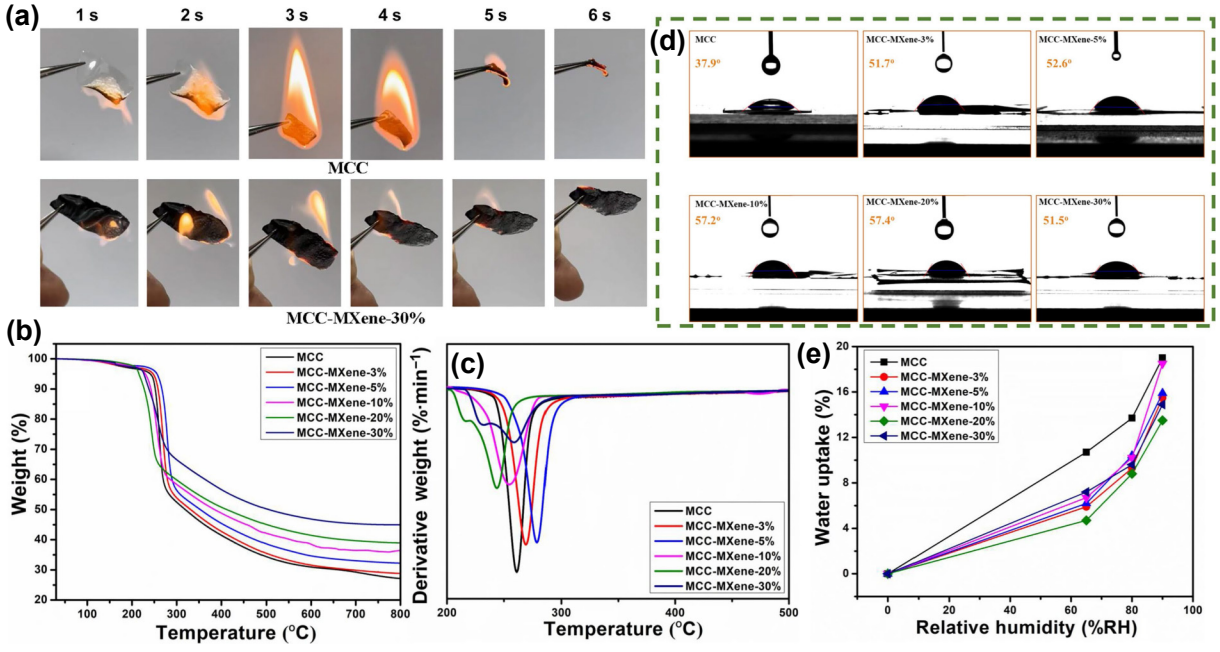

Figure 7 (a) Burning state at different times for MCC and MCC–MXene-30% nanocomposite films on a fire lamp. (b) TGA curves and (c) DTG curves of neat MCC and MCC–MXene nanocomposite films with different MXene contents under a nitrogen atmosphere. (d) Contact angle measurements for neat MCC and MCC–MXene nanocomposite films with different MXene contents. (e) Water uptake of neat MCC and MCC–MXene nanocomposite films at various RHs.

an effective physical barrier to prevent the rapid combustion of MCC [80, 81].

3.6 Water resistance and antibacterial property

Water resistance is crucial for maintaining the stability of the dielectric properties of nanocomposite films. Therefore, in this study, the water absorption properties of the pristine MCC and MCC–MXene nanocomposite films were investigated, and the results are displayed in Fig. 7(e). The water absorption capacities are 10.7%, 5.9%, 6.2%, 6.7%, 4.7%, and 7.2%, respectively, under 65% RH for the MCC, MCC–MXene-3%, MCC–MXene-5%, MCC–MXene-10%, MCC–MXene-20%, and MCC–MXene-30%. The results show that the introduction of MXene effectively reduces the water absorption capacity, suggesting that the proposed DMAc/LiCl system is beneficial for controlling the water absorption of MCC–MXene nanocomposite films. The excellent compatibility and close contact between the MCC and MXene nanosheets reported in this study are beneficial for preventing water uptake. In addition, after the introduction of MXene, the contact angle of the MCC–MXene nanocomposite film increases from 37.9° for the pure MCC film to more than 50° for the nanocomposite film (Fig. 7(d)), and with an increase in the MXene content, an overall increasing trend is shown. It may be because, first, the inherent contact angle of MXene is larger than that of the particularly hydrophilic cellulose, so the contact angle of the nanocomposite films can be improved after doping. Second, the contact angle of MXene is further enhanced owing to the possible change in the surface environment of MXene through TBAOH intercalation (as confirmed by XPS analysis). Zhang et al. reported that MXene has a water contact angle of 59.9°, which suggests its hydrophilicity [45]. Owing to the TBAOH intercalation process, which possibly replaced some –OH groups, MXene–TBAOH attained a water contact angle of 119.1°. The above characteristics contribute to the improvement in the contact angle of the nanocomposite films. These unique properties have the potential to expand the use of MCC–MXenes in wet environments for portable and wearable electronic devices.

To investigate the antibacterial efficiency of the MCC–MXene nanocomposite film, the inhibitory effects of three materials (MXene, MCC, and MCC–MXene-30%) were examined against *B. subtilis*. To evaluate the antibacterial activity of pure MXene in growth media, *B. subtilis* bacterial strains were exposed to 1.9 mg·mL^{-1} of MXene nanosheets (synthesized using the MILD method) in an LB medium for 5 h. Figure S14 in the ESM shows typical photographs of *B. subtilis* bacterial colonies after treatment with MXene. Compared with that of the control, the number of colonies significantly decreases when exposed to MXene nanosheets. This is consistent with the results reported by Rasool et al. that MXenes have antibacterial properties [82]. The research team proposed that the antibacterial mechanism of MXene is that MXene nanosheets interact with the cell membrane through hydrogen bonding to inhibit the uptake of nutrients by bacteria, resulting in antibacterial properties. In addition, the contact of bacteria with the sharp edge of MXene nanosheets can destroy the bacterial membrane, which can also lead to antibacterial properties. Based on the above results, MXene is confirmed to have antibacterial properties. Therefore, we need to prove that the introduction of MXene into MCC can make the MCC–MXene nanocomposite film possess certain antibacterial properties. As can be observed from Fig. S14 in the ESM, MCC–MXene-30% exhibits a certain degree of antibacterial performance compared with pure MCC, even though not as excellent as MXene nanosheets. This may be due to the insufficient contact between the nanosheets and bacteria after fabricating MCC and MXene into nanocomposite films, so that the antibacterial properties of the nanosheets cannot be fully exploited. However, because of the existence of MXene in our synthesized nanocomposite films, on the one hand, bacteria can contact MXene on the surface of the film but on the other hand, during long-term contact with bacteria, they may penetrate into the membrane, which gives the nanocomposite films a certain degree of antibacterial properties. Cellulose is a biomass material that may easily breed bacteria. Therefore, cellulose-based composite films with certain antibacterial properties are important for the long-term use of electronic devices [83].

3.7 Stability of MXene/DMAc and MCC–MXene/DMAc-LiCl

The stability of MXene was determined using UV–vis spectroscopy. As depicted in Fig. 8(b) and Fig. S15(b) in the ESM, after 28 days of storage at room temperature, 96.4% of the

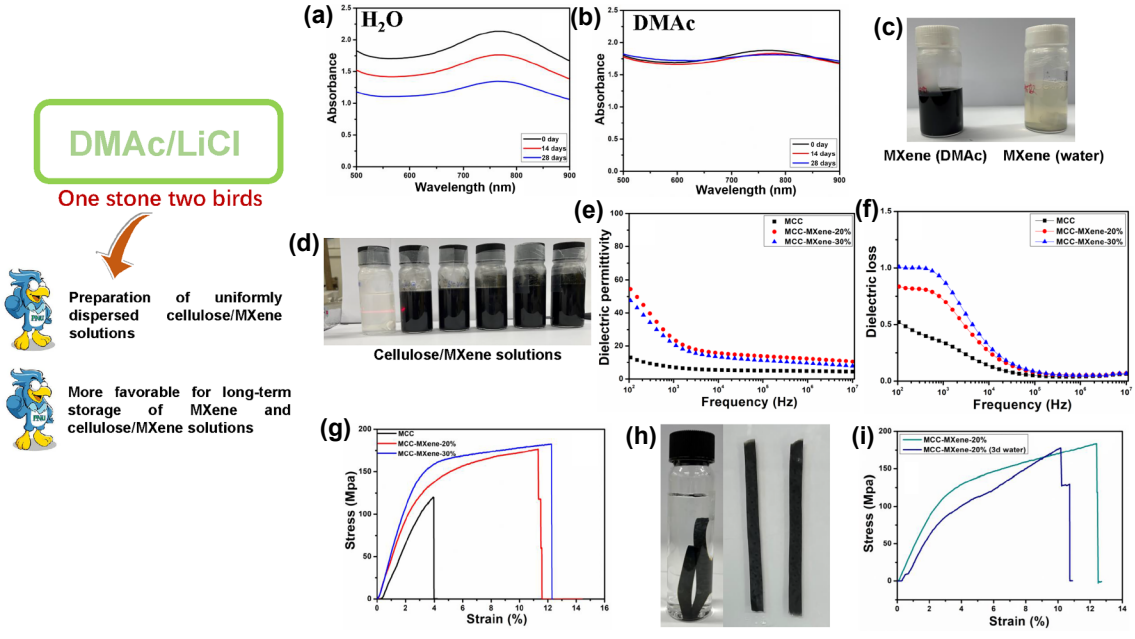

Figure 8 (a) UV–vis peaks at λ = 785 nm of MXene after storage in water for different times. (b) UV–vis peaks at λ = 785 nm of MXene after storage in DMAc for different times. (c) Photographs of lower concentrations of MXene (DMAc) and MXene (water) after long-term storage. (d) Photographs of MCC and MCC–MXene mixed solutions after storage for 2 months. (e) Permittivity of MCC–MXene nanocomposite films (prepared from solutions stored for 2 months). (f) Dielectric loss of MCC–MXene nanocomposite films (prepared from solutions stored for 2 months). (g) Stress–strain curves of MCC–MXene nanocomposite films (prepared from solutions stored for 2 months). (h) Photographs of MCC–MXene-20% soaked in water for 3 days and dried after soaking. (i) Stress–strain curves of the original MCC–MXene-20% and MCC–MXene-20% after soaking in water for 3 days.

absorbance was detected compared to the absorbance of the initial MXene dispersion, indicating that the change in concentration of the MXene nanosheets dispersed in DMAc is extremely small. For comparison, we performed the same stability experiments using water-dispersed MXene synthesized using the MILD method. As indicated in Fig. 8(a) and Fig. S15(a) in the ESM, after storage at room temperature for 28 days, only 63.0% of the absorbance was detected compared to the absorbance of the initial MXene dispersion, indicating that the concentration of MXene nanosheets dispersed in water synthesized by MILD method is significantly reduced because of the large amount of MXene being oxidized. In addition, we prepared MXene dispersions with a lower concentration. From Fig. 8(c), we can see that the color of MXene dispersed in water becomes clear after 60 days of storage, and it is almost completely oxidized. However, the color of MXene dispersed in DMAc is still black and contains a large amount of MXene. The superior oxidation resistance of MXene dispersed in DMAc may be attributed to two factors: (1) The surface environment of the resulting MXene after intercalation with TBAOH changes, making it less susceptible to oxidation (according to the XPS results). (2) The amount of dissolved oxygen in the DMAc organic solvent is small, which is beneficial for protecting MXene from rapid oxidation. Stable preservation of MXene dispersions is crucial for the preparation of large-scale nanocomposites in the future [45].

We used a DMAc/LiCl solvent system to dissolve MCC and dispersed MXene into this solution. The DMAc/LiCl solvent system achieves two benefits (one stone two birds) in the preparation of nanocomposite dispersions. First, DMAc/LiCl is an excellent solvent system for dissolving MCC. Because of the existence of Li^+ and Cl^- electron pairs in DMAc/LiCl, when MCC is dissolved in the DMAc/LiCl solvent system, Cl^- forms a strong hydrogen bond with the hydroxyl protons of cellulose, thereby forming an intermolecular hydrogen-bond network. In this process, the intramolecular hydrogen bonds of cellulose are broken, and simultaneously, the Li^+–Cl^- ion pair is split. Then, the Li^+ cations are solvated by the free DMAc molecules, and the further solvated Li^+ cations are accompanied by the hydrogen bonds of Cl^- to reach electrical equilibrium [84]. Therefore, MCC can be completely dispersed into the DMAc/LiCl system to form a homogeneous solution. Second, because we obtained MXene nanosheets that can be stably dispersed and preserved in DMAc by the TBAOH intercalation method, choosing DMAc/LiCl instead of water/urea/NaOH as the solvent greatly improves the compatibility between cellulose and MXene. The improved compatibility ensures better permittivity and mechanical properties. In addition, Wang et al. reported that inorganic salts (such as LiCl and NaCl) can significantly reduce both the water activity and concentration of dissolved oxygen in aqueous solutions [43]. Therefore, we hypothesized that the presence of LiCl in our system might further protect the MXene from oxidation after long-term storage. We prepared typical MCC–MXene nanocomposite films using MCC–MXene solutions stored for 2 months (Fig. 8(d)). It is evident that MCC–MXene nanocomposite films are successfully obtained even after 2 months of storage in the MCC–MXene solution, as depicted by the FTIR spectra (Fig. S16 in the ESM). The formation of hydrogen bonds is confirmed in Fig. S16(b) in the ESM, which also indicates the successful synthesis of nanocomposite films. Moreover, as shown in Figs. 8(e) and 8(f), the dielectric properties of the nanocomposite films prepared after storing the MCC–MXene solution for two months are not compromised. Furthermore, the mechanical properties are comparable to those of the nanocomposite films prepared from a fresh solution (Fig. 8(g) and Fig. S17 in the ESM).

To prove that the prepared nanocomposite films can be used stably under high-humidity conditions and the structure will not be damaged, we soaked the nanocomposite films in water for 3 days (Fig. 8(h)), dried them, and tested their relative performance changes. As displayed in Fig. S19 in the ESM, the hydrogen bonds are still detectable after soaking in water for 3 days, indicating that the structure of the nanocomposite film is not damaged. Even after 3 days of immersion in water, the mechanical properties are not significantly compromised (Fig. 8(i) and Table S5 in the ESM).

Figure S18 in the ESM presents the photos of MCC–MXene-20% soaked in water for 3 and 30 days. The nanocomposite film is not broken after soaking in water for 30 days, but the MXene immersed in water for a long time may oxidize, resulting in color change. These foldable MCC–MXene films with outstanding durability and stability are expected to be advantageous for electronic device applications.

4 Conclusion

We demonstrated an efficient method for fabricating MCC–MXene nanocomposite films with excellent properties using DMAc/LiCl as the solvent system. Two-dimensional MXene nanosheets with good dispersibility in DMAc were synthesized via facile TBAOH-assisted intercalation. The introduction of MXene nanosheets into the MCC matrix increased not only the permittivity of the nanocomposite film owing to the microscopic dipole and microcapacitor network formation, but also the thermal conductivity because of the excellent dispersion state of the MXene nanosheets that provided a continuous thermal conductive network in the in-plane direction of the nanocomposite films. At 10^2 kHz, when the MXene content is 20 wt.%, although the permittivity of flexible nanocomposite film increases by 8.7 times (from 8.2 to 71.4), the dielectric loss of the nanocomposite film only increases by 1.8 times (from 0.39 to 0.70). The in-plane thermal conductivity reaches 8.523 and 9.668 $W \cdot m^{-1} \cdot K^{-1}$ with 20 wt.% and 30 wt.% MXene loading, respectively. Simultaneously, the mechanical properties, thermal stability, antibacterial activity, and water resistance of the nanocomposite films all show considerable improvements after uniform introduction of MXene nanosheets, which warrants the application of MCC–MXene nanocomposite films in real environments. More importantly, owing to the excellent dispersion of MXene nanosheets in DMAc and long-term storage without oxidation, the use of DMAc/LiCl as the solvent system for mixing MCC and MXene is beneficial for the compatibility of MXene and MCC, which is essential for obtaining uniform nanocomposite materials. Furthermore, with the acceptable oxidation resistance of MXene in DMAc, the developed preparation strategy will have more practical application prospects.

Acknowledgements

The work was supported by the National Research Foundation of Korea (NRF) Grant funded by the Ministry of Science and ICT, Korea (NRF-2021R1I1A3060098; NRF-2021R1I1A3059777). The work was supported by the Brain Korea 21 Plus Program (4199990414196) and the Korea Institute for Advancement of Technology funded by the Ministry of Trade, Industry and Energy (P0017531). Y. Z. Y. was partially supported by the China Scholarship Council (No. 201908260073).

Electronic Supplementary Material: Supplementary material (preparation of water-dispersible MXene; SEM and HR-TEM image of the Ti_3AlC_2, multilayer $Ti_3C_2T_x$ (M-MXene); TEM images of $Ti_3C_2T_x$ MXene nanosheets; XPS spectra of M-MXene and MXene-TBAOH; low-resolution fractured crosssectional SEM images and SEM–EDX mapping micrographs of key samples; atomic force microscopy images and XRD patterns of MCC–MXene nanocomposite films; detailed peak positions of O–H characteristic peaks of MCC–MXene nanocomposite films (FTIR); photographs of agar plates onto *B. subtilis* bacterial cells (after treatment for 5 h with MXene (MILD), MCC, and MCC–MXene-30%); changes in absorbance of MXene in water and DMAc; FTIR spectra and mechanical properties of MCC and MCC–MXene nanocomposite films (prepared from the solutions stored for 2 months); photographs of MCC–MXene-20% soaked in water for 3 and 30 days; FTIR spectra of neat MCC, MCC–MXene-5%, and MCC–MXene-20% nanocomposite films (after 3 days of immersion in water); tables of CTE values and tensile properties of MCC–MXene nanocomposite films; comparison tables of permittivity, dielectric loss, and in-plane thermal conductivity values of MCC–MXene nanocomposite films with those of other reported cellulose-based nanocomposites or composites containing MXene fillers) is available in the online version of this article at https://doi.org/10.1007/s12274-022-5062-3.

References

[1] Li, L.; Cheng, J. S.; Cheng, Y. Y.; Han, T.; Liu, Y.; Zhou, Y.; Zhao, G. H.; Zhao, Y.; Xiong, C. X.; Dong, L. J. et al. Significant improvements in dielectric constant and energy density of ferroelectric polymer nanocomposites enabled by ultralow contents of nanofillers. *Adv. Mater.* **2021**, *33*, 2102392.

[2] Feng, Q. K.; Zhong, S. L.; Pei, J. Y.; Zhao, Y.; Zhang, D. L.; Liu, D. F.; Zhang, Y. X.; Dang, Z. M. Recent progress and future prospects on all-organic polymer dielectrics for energy storage capacitors. *Chem. Rev.* **2022**, *122*, 3820–3878.

[3] Luo, H.; Zhou, X. F.; Ellingford, C.; Zhang, Y.; Chen, S.; Zhou, K. C.; Zhang, D.; Bowen, C. R.; Wan, C. Y. Interface design for high energy density polymer nanocomposites. *Chem. Soc. Rev.* **2019**, *48*, 4424–4465.

[4] Zhao, D. W.; Zhu, Y.; Cheng, W. K.; Chen, W. S.; Wu, Y. Q.; Yu, H. P. Cellulose-based flexible functional materials for emerging intelligent electronics. *Adv. Mater.* **2021**, *33*, 2000619.

[5] Sun, Z.; Qu, K. Q.; You, Y.; Huang, Z. H.; Liu, S. X.; Li, J.; Hu, Q.; Guo, Z. H. Overview of cellulose-based flexible materials for supercapacitors. *J. Mater. Chem. A* **2021**, *9*, 7278–7300.

[6] Wang, X. D.; Yao, C. H.; Wang, F.; Li, Z. D. Cellulose-based nanomaterials for energy applications. *Small* **2017**, *13*, 1702240.

[7] Yang, D.; Kong, X. X.; Ni, Y. F.; Gao, D. H.; Yang, B.; Zhu, Y. Y.; Zhang, L. Q. Novel nitrile-butadiene rubber composites with enhanced thermal conductivity and high dielectric constant. *Compos. Part A Appl. Sci. Manuf.* **2019**, *124*, 105447.

[8] Zhang, X. H.; Tan, C.; Ma, Y. H.; Wang, F.; Yang, W. T. $BaTiO_3$@carbon/silicon carbide/poly(vinylidene fluoride-hexafluoropropylene) three-component nanocomposites with high dielectric constant and high thermal conductivity. *Compos. Sci. Technol.* **2018**, *162*, 180–187.

[9] He, D. L.; Wang, Y.; Song, S. L.; Liu, S.; Deng, Y. Significantly enhanced dielectric performances and high thermal conductivity in poly(vinylidene fluoride)-based composites enabled by SiC@SiO_2 core-shell whiskers alignment. *ACS Appl. Mater. Interfaces* **2017**, *9*, 44839–44846.

[10] Budzalek, K.; Ding, H. J.; Janasz, L.; Wypych-Puszkarz, A.; Cetinkaya, O.; Pietrasik, J.; Kozanecki, M.; Ulanski, J.; Matyjaszewski, K. Star polymer−TiO_2 nanohybrids to effectively modify the surface of PMMA dielectric layers for solution processable OFETs. *J. Mater. Chem. C* **2021**, *9*, 1269–1278.

[11] Su, Y. T.; Zhang, W. Q.; Lan, J. L.; Sui, G.; Zhang, H. T.; Yang, X. P. Flexible reduced graphene oxide/polyacrylonitrile dielectric nanocomposite films for high-temperature electronics applications. *ACS Appl. Nano Mater.* **2020**, *3*, 7005–7015.

[12] Yan, Y. Z.; Park, S. S.; Moon, H. R.; Zhang, W. J.; Yuan, S.; Shi, L. Y.; Seong, D. G.; Ha, C. S. Thermally robust zirconia nanorod/polyimide hybrid films as a highly flexible dielectric material. *ACS Appl. Nano Mater.* **2021**, *4*, 8217–8230.

[13] Park, J. H.; Oh, J. Y.; Han, S. W.; Lee, T. I.; Baik, H. K. Low-temperature, solution-processed ZrO_2:B thin film: A bifunctional inorganic/organic interfacial glue for flexible thin-film transistors. *ACS Appl. Mater. Interfaces* **2015**, *7*, 4494–4503.

[14] Yang, Y. Y.; Zhao, Y. S.; Liu, J.; Nie, Z. K.; Ma, J.; Hua, M. T.; Zhang, Y. C.; Cai, X. F.; He, X. M. Flexible and transparent high-dielectric-constant polymer films based on molecular ferroelectric-modified poly(vinyl alcohol). *ACS Materials Lett.* **2020**, *2*, 453–460.

[15] Alghamdi, H. M.; Rajeh, A. Synthesis of carbon nanotubes/titanium

dioxide and study of its effect on the optical, dielectric, and mechanical properties of polyvinyl alcohol/sodium alginate for energy storage devices. *Int. J. Energy Res.*, in press, https://doi.org/10.1002/er.7578.

[16] Chen, Y. W.; Liu, Y. H.; Xia, Y. M.; Liu, X. Q.; Qiang, Z.; Yang, J. Y.; Zhang, B. L.; Hu, Z. D.; Wang, Q.; Wu, W. F. et al. Electric field-induced assembly and alignment of silver-coated cellulose for polymer composite films with enhanced dielectric permittivity and anisotropic light transmission. *ACS Appl. Mater. Interfaces* **2020**, *12*, 24242–24249.

[17] Chen, L. M.; Abdalkarim, S. Y. H.; Yu, H. Y.; Chen, X.; Tang, D. P.; Li, Y. Z.; Tam, K. C. Nanocellulose-based functional materials for advanced energy and sensor applications. *Nano Res.* **2022**, *15*, 7432–7452.

[18] Wang, Z. H.; Lee, Y. H.; Kim, S. W.; Seo, J. Y.; Lee, S. Y.; Nyholm, L. Why cellulose-based electrochemical energy storage devices? *Adv. Mater.* **2021**, *33*, 2000892.

[19] Zhang, C. L.; Cha, R. T.; Zhang, P.; Luo, H. Z.; Jiang, X. Y. Cellulosic substrate materials with multi-scale building blocks: Fabrications, properties and applications in bioelectronic devices. *Chem. Eng. J.* **2022**, *430*, 132562.

[20] Lu, J. L.; Hu, S. M.; Li, W. R.; Wang, X. F.; Mo, X. W.; Gong, X. T.; Liu, H.; Luo, W.; Dong, W.; Sima, C. T. et al. A Biodegradable and recyclable piezoelectric sensor based on a molecular ferroelectric embedded in a bacterial cellulose hydrogel. *ACS Nano* **2022**, *16*, 3744–3755.

[21] Luo, S. B.; Shen, Y. B.; Yu, S. H.; Wan, Y. J.; Liao, W. H.; Sun. R.; Wong, C. P. Construction of a 3D-$BaTiO_3$ network leading to significantly enhanced dielectric permittivity and energy storage density of polymer composites. *Energy Environ. Sci.* **2017**, *10*, 137–144.

[22] Beaulieu, M. R.; Baral, J. K.; Hendricks, N. R.; Tang, Y. Y.; Briseño, A. L.; Watkins, J. J. Solution processable high dielectric constant nanocomposites based on ZrO_2 nanoparticles for flexible organic transistors. *ACS Appl. Mater. Interfaces* **2013**, *5*, 13096–13103.

[23] Kim, J. O.; Hur, J. S.; Kim, D.; Lee, B.; Jung, J. M.; Kim, H. A.; Chung, U. J.; Nam, S. H.; Hong, Y.; Park, K. S. et al. Network structure modification-enabled hybrid polymer dielectric film with zirconia for the stretchable transistor applications. *Adv. Funct. Mater.* **2020**, *30*, 1906647.

[24] Zhang, D.; Liu, W. W.; Guo, R.; Zhou, K. C.; Luo, H. High discharge energy density at low electric field using an aligned titanium dioxide/lead zirconate titanate nanowire array. *Adv. Sci.* **2018**, *5*, 1700512.

[25] Qian, C.; Zhu, T. W.; Zheng, W. W.; Bei, R. X.; Liu, S. W.; Yu, D. S.; Chi, Z. G.; Zhang, Y.; Xu, J. R. Improving dielectric properties and thermostability of $CaCu_3Ti_4O_{12}$/polyimide composites by employing surface hydroxylated $CaCu_3Ti_4O_{12}$ particles. *ACS Appl. Polym. Mater.* **2019**, *1*, 1263–1271.

[26] Chen, J. W.; Wang, X. C.; Yu, X. M.; Yao, L. M.; Duan, Z. K.; Fan, Y.; Jiang, Y. W.; Zhou, Y. X.; Pan, Z. B. High dielectric constant and low dielectric loss poly(vinylidene fluoride) nanocomposites via a small loading of two-dimensional Bi_2Te_3@Al_2O_3 hexagonal nanoplates. *J. Mater. Chem. C* **2018**, *6*, 271–279.

[27] Su, Y. T.; Zhou, M. P.; Sui, G.; Lan, J. L.; Zhang, H. T.; Yang, X. P. Polyvinyl butyral composites containing halloysite nanotubes/reduced graphene oxide with high dielectric constant and low loss. *Chem. Eng. J.* **2020**, *394*, 124910.

[28] Mao, H. J.; Liu, D. F.; Zhang, N.; Huang, T.; Kühnert, I.; Yang, J. H.; Wang, Y. Constructing a microcapacitor network of carbon nanotubes in polymer blends via crystallization-induced phase separation toward high dielectric constant and low loss. *ACS Appl. Mater. Interfaces* **2020**, *12*, 26444–26454.

[29] Tu, S. B.; Jiang, Q.; Zhang, X. X.; Alshareef, H. N. Large dielectric constant enhancement in MXene percolative polymer composites. *ACS Nano* **2018**, *12*, 3369–3377.

[30] Mirkhani, S. A.; Zeraati, A. S.; Aliabadian, E.; Naguib, M.; Sundararaj, U. High dielectric constant and low dielectric loss via poly(vinyl alcohol)/$Ti_3C_2T_x$ MXene nanocomposites. *ACS Appl. Mater. Interfaces* **2019**, *11*, 18599–18608.

[31] Zeraati, A. S.; Arjmand, M.; Sundararaj, U. Silver nanowire/MnO_2 nanowire hybrid polymer nanocomposites: Materials with high dielectric permittivity and low dielectric loss. *ACS Appl. Mater. Interfaces* **2017**, *9*, 14328–14336.

[32] Ma, W. J.; Yang, K.; Wang, H. Y.; Li, H. F. Poly(vinylidene fluoride-*co*-hexafluoropropylene)-MXene nanosheet composites for microcapacitors. *ACS Appl. Nano Mater.* **2020**, *3*, 7992–8003.

[33] Wan, S. J.; Li, X.; Chen, Y.; Liu, N. N.; Du, Y.; Dou, S. X.; Jiang, L.; Cheng, Q. F. High-strength scalable MXene films through bridging-induced densification. *Science* **2021**, *374*, 96–99.

[34] Hu, D. W.; Wang, S. Q.; Zhang, C.; Yi, P. S.; Jiang, P. K.; Huang, X. Y. Ultrathin MXene-aramid nanofiber electromagnetic interference shielding films with tactile sensing ability withstanding harsh temperatures. *Nano Res.* **2021**, *14*, 2837–2845.

[35] Wang, D. Z.; Wei, H.; Lin, Y.; Jiang, P. K.; Bao, H.; Huang, X. Y. Achieving ultrahigh thermal conductivity in Ag/MXene/epoxy nanocomposites via filler−filler interface engineering. *Compos. Sci. Technol.* **2021**, *213*, 108953.

[36] Tu, S. B.; Jiang, Q.; Zhang, J. W.; He, X.; Hedhili, M. N.; Zhang, X. X.; Alshareef, H. N. Enhancement of dielectric permittivity of $Ti_3C_2T_x$ MXene/polymer composites by controlling flake size and surface termination. *ACS Appl. Mater. Interfaces* **2019**, *11*, 27358–27362.

[37] Jin, X. X.; Wang, J. F.; Dai, L. Z.; Liu, X. Y.; Li, L.; Yang, Y. Y.; Cao, Y. X.; Wang, W. J.; Wu, H.; Guo, S. Y. Flame-retardant poly(vinyl alcohol)/MXene multilayered films with outstanding electromagnetic interference shielding and thermal conductive performances. *Chem. Eng. J.* **2020**, *380*, 122475.

[38] Liu, R.; Li, W. H. High-thermal-stability and high-thermal-conductivity $Ti_3C_2T_x$ MXene/poly(vinyl alcohol) (PVA) composites. *ACS Omega* **2018**, *3*, 2609–2617.

[39] Balandin, A. A.; Ghosh, S.; Bao, W. Z.; Calizo, I.; Teweldebrhan, D.; Miao, F.; Lau, C. N. Superior thermal conductivity of single-layer graphene. *Nano Lett.* **2008**, *8*, 902–907.

[40] Chen, H. Y.; Ginzburg, V. V.; Yang, J.; Yang, Y. F.; Liu, W.; Huang, Y.; Du, L. B.; Chen, B. Thermal conductivity of polymer-based composites: Fundamentals and applications. *Prog. Polym. Sci.* **2016**, *59*, 41–85.

[41] Zhou, Z. H.; Song, Q. C.; Huang, B. X.; Feng, S. Y.; Lu, C. H. Facile fabrication of densely packed Ti_3C_2 MXene/nanocellulose composite films for enhancing electromagnetic interference shielding and electro-/photothermal performance. *ACS Nano* **2021**, *15*, 12405–12417.

[42] Sun, K.; Wang, F.; Yang, W. K.; Liu, H.; Pan, C. F.; Guo, Z. H.; Liu, C. T.; Shen, C. Y. Flexible conductive polyimide fiber/MXene composite film for electromagnetic interference shielding and joule heating with excellent harsh environment tolerance. *ACS Appl. Mater. Interfaces* **2021**, *13*, 50368–50380.

[43] Wang, X. Y.; Wang, Z. Y.; Qiu, J. S. Stabilizing MXene by hydration chemistry in aqueous solution. *Angew. Chem., Int. Ed.* **2021**, *60*, 26587–26591.

[44] Doo, S.; Chae, A.; Kim, D.; Oh, T.; Ko, T. Y.; Kim, S. J.; Koh, D. Y.; Koo, C. M. Mechanism and kinetics of oxidation reaction of aqueous $Ti_3C_2T_x$ suspensions at different pHs and temperatures. *ACS Appl. Mater. Interfaces* **2021**, *13*, 22855–22865.

[45] Zhang, Q. X.; Lai, H. R.; Fan, R. Z.; Ji, P. Y.; Fu, X. L.; Li, H. High concentration of $Ti_3C_2T_x$ MXene in organic solvent. *ACS Nano* **2021**, *15*, 5249–5262.

[46] Kim, D.; Ko, T. Y.; Kim, H.; Lee, G. H.; Cho, S.; Koo, C. M. Nonpolar organic dispersion of 2D $Ti_3C_2T_x$ MXene flakes via simultaneous interfacial chemical grafting and phase transfer method. *ACS Nano* **2019**, *13*, 13818–13828.

[47] Iqbal, A.; Hong, J.; Ko, T. Y.; Koo, C. M. Improving oxidation stability of 2D MXenes: Synthesis, storage media, and conditions. *Nano Converg.* **2021**, *8*, 9.

[48] Tang, X. W.; Murali, G.; Lee, H.; Park, S.; Lee, S.; Oh, S. M.; Lee, J.; Ko, T. Y.; Koo, C. M.; Jeong, Y. J. et al. Engineering aggregation-resistant MXene nanosheets as highly conductive and stable inks for all-printed electronics. *Adv. Funct. Mater.* **2021**, *31*, 2010897.

[49] Alhabeb, M.; Maleski, K.; Anasori, B.; Lelyukh, P.; Clark, L.; Sin, S.; Gogotsi, Y. Guidelines for synthesis and processing of two-dimensional titanium carbide ($Ti_3C_2T_x$ MXene). *Chem. Mater.* **2017**, *29*, 7633–7644.

[50] Chen, J. N.; Yuan, X. L.; Lyu, F. L.; Zhong, Q. X.; Hu, H. C.; Pan, Q.; Zhang, Q. Integrating MXene nanosheets with cobalt-tipped

carbon nanotubes for an efficient oxygen reduction reaction. *J. Mater. Chem. A* **2019**, *7*, 1281–1286.
[51] Wan, Y. Z.; Xiong, P. X.; Liu, J. Z.; Feng, F. F.; Xun, X. W.; Gama, F. M.; Zhang, Q. C.; Yao, F. L.; Yang, Z. W.; Luo, H. L. et al. Ultrathin, strong, and highly flexible $Ti_3C_2T_x$ MXene/bacterial cellulose composite films for high-performance electromagnetic interference shielding. *ACS Nano* **2021**, *15*, 8439–8449.
[52] Xue, Y. J.; Feng, J. B.; Huo, S. Q.; Song, P. A.; Yu, B.; Liu, L.; Wang, H. Polyphosphoramide-intercalated MXene for simultaneously enhancing thermal stability, flame retardancy and mechanical properties of polylactide. *Chem. Eng. J.* **2020**, *397*, 125336.
[53] Halim, J.; Cook, K. M.; Eklund, P.; Rosen, J.; Barsoum, M. W. XPS of cold pressed multilayered and freestanding delaminated 2D thin films of $Mo_2TiC_2T_z$ and $Mo_2Ti_2C_3T_z$ (MXenes). *Appl. Surf. Sci.* **2019**, *494*, 1138–1147.
[54] Karmakar, K.; Sarkar, P.; Sultana, J.; Kurra, N.; Rao, K. D. M. Layer-by-layer assembly-based heterointerfaces for modulating the electronic properties of $Ti_3C_2T_x$ MXene. *ACS Appl. Mater. Interfaces* **2021**, *13*, 59104–59114.
[55] Cao, W. T.; Ma, C.; Mao, D. S.; Zhang, J.; Ma, M. G.; Chen, F. MXene-reinforced cellulose nanofibril inks for 3D-printed smart fibres and textiles. *Adv. Funct. Mater.* **2019**, *29*, 1905898.
[56] French, A. D. Idealized powder diffraction patterns for cellulose polymorphs. *Cellulose* **2014**, *21*, 885–896.
[57] Shin, I.; Postnova, I.; Shchipunov, Y.; Ha, C. S. Transparent regenerated cellulose bionanocomposite film reinforced by exfoliated montmorillonite with polyhedral oligomeric silsesquioxane bearing amino groups. *Compos. Interfaces* **2021**, *28*, 653–669.
[58] Wang, S. R.; Tambraparni, M.; Qiu, J. J.; Tipton, J.; Dean, D. Thermal expansion of graphene composites. *Macromolecules* **2009**, *42*, 5251–5255.
[59] Du, J. H.; Cheng, H. M. The fabrication, properties, and uses of graphene/polymer composites. *Macromol. Chem. Phys.* **2012**, *213*, 1060–1077.
[60] Cao, W. T.; Chen, F. F.; Zhu, Y. J.; Zhang, Y. G.; Jiang, Y. Y.; Ma, M. G.; Chen, F. Binary strengthening and toughening of MXene/cellulose nanofiber composite paper with nacre-inspired structure and superior electromagnetic interference shielding properties. *ACS Nano* **2018**, *12*, 4583–4593.
[61] Zhou, Z. H.; Liu, J. Z.; Zhang, X. X.; Tian, D.; Zhan, Z. Y.; Lu, C. H. Ultrathin MXene/calcium alginate aerogel film for high-performance electromagnetic interference shielding. *Adv. Mater. Interfaces* **2019**, *6*, 1802040.
[62] Rana, S. M. S.; Rahman, M. T.; Salauddin, M.; Sharma, S.; Maharjan, P.; Bhatta, T.; Cho, H.; Park, C.; Park, J. Y. Electrospun PVDF-TrFE/MXene nanofiber mat-based triboelectric nanogenerator for smart home appliances. *ACS Appl. Mater. Interfaces* **2021**, *13*, 4955–4967.
[63] Deng, Q. H.; Zhou, F. R.; Qin, B.; Feng, Y. F.; Xu, Z. C. Eco-friendly poly(vinyl alcohol)/delaminated V_2C MXene high-*k* nanocomposites with low dielectric loss enabled by moderate polarization and charge density at the interface. *Ceram. Int.* **2020**, *46*, 27326–27335.
[64] Li, W. Y.; Song, Z. Q.; Zhong, J. M.; Qian, J.; Tan, Z. Y.; Wu, X. Y.; Chu, H. Y.; Nie, W.; Ran, X. H. Multilayer-structured transparent MXene/PVDF film with excellent dielectric and energy storage performance. *J. Mater. Chem. C* **2019**, *7*, 10371–10378.
[65] Yu, S. Q.; Ding, C. L.; Liu, Y.; Liu, Y.; Zhang, Y.; Luo, H.; Zhang, D.; Chen, S. Enhanced breakdown strength and energy density over a broad temperature range in polyimide dielectrics using oxidized MXenes filler. *J. Power Sources* **2022**, *535*, 231415.
[66] Yin, Y. A.; Zhang, C. G.; Chen, J. S.; Yu, W. C.; Shi, Z. Q.; Xiong, C. X.; Yang, Q. L. Cellulose/$BaTiO_3$ nanofiber dielectric films with enhanced energy density by interface modification with poly(dopamine). *Carbohydr. Polym.* **2020**, *249*, 116883.
[67] Zhang, C. G.; Yin, Y. A.; Yang, Q. L.; Shi, Z. Q.; Hu, G. H.; Xiong, C. X. Flexible cellulose/$BaTiO_3$ nanocomposites with high energy density for film dielectric capacitor. *ACS Sustain. Chem. Eng.* **2019**, *7*, 10641–10648.
[68] Wang, F. J.; Wang, M. H.; Shao, Z. Q. Dispersion of reduced graphene oxide with montmorillonite for enhancing dielectric properties and thermal stability of cyanoethyl cellulose nanocomposites. *Cellulose* **2018**, *25*, 7143–7152.
[69] Lao, J. P.; Xie, H. A.; Shi, Z. Q.; Li, G.; Li, B.; Hu, G. H.; Yang, Q. L.; Xiong, C. X. Flexible regenerated cellulose/boron nitride nanosheet high-temperature dielectric nanocomposite films with high energy density and breakdown strength. *ACS Sustain. Chem. Eng.* **2018**, *6*, 7151–7158.
[70] Tao, J.; Cao, S. A. Flexible high dielectric thin films based on cellulose nanofibrils and acid oxidized multi-walled carbon nanotubes. *RSC Adv.* **2020**, *10*, 10799–10805.
[71] Tao, J.; Cao, S. A.; Liu, W.; Deng, Y. L. Facile preparation of high dielectric flexible films based on titanium dioxide and cellulose nanofibrils. *Cellulose* **2019**, *26*, 6087–6098.
[72] Yang, W. X.; Zhao, Z. D.; Wu, K.; Huang, R.; Liu, T. Y.; Jiang, H.; Chen, F.; Fu, Q. Ultrathin flexible reduced graphene oxide/cellulose nanofiber composite films with strongly anisotropic thermal conductivity and efficient electromagnetic interference shielding. *J. Mater. Chem. C* **2017**, *5*, 3748–3756.
[73] Song, N.; Hou, X. S.; Chen, L.; Cui, S. Q.; Shi, L. Y.; Ding, P. A green plastic constructed from cellulose and functionalized graphene with high thermal conductivity. *ACS Appl. Mater. Interfaces* **2017**, *9*, 17914–17922.
[74] Song, N.; Cao, D. L.; Luo, X.; Guo, Y. Q.; Gu, J. W.; Ding, P. Aligned cellulose/nanodiamond plastics with high thermal conductivity. *J. Mater. Chem. C* **2018**, *6*, 13108–13113.
[75] Wang, X. W.; Wu, P. Y. Fluorinated carbon nanotube/nanofibrillated cellulose composite film with enhanced toughness, superior thermal conductivity, and electrical insulation. *ACS Appl. Mater. Interfaces* **2018**, *10*, 34311–34321.
[76] Song, G. C.; Kang, R. Y.; Guo, L. C.; Ali, Z.; Chen, X. Y.; Zhang, Z. Y.; Yan, C.; Lin, C. T.; Jiang, N.; Yu, J. H. Highly flexible few-layer Ti_3C_2 MXene/cellulose nanofiber heat-spreader films with enhanced thermal conductivity. *New J. Chem.* **2020**, *44*, 7186–7193.
[77] Gao, Q. S.; Pan, Y. M.; Zheng, G. Q.; Liu, C. T.; Shen, C. Y.; Liu, X. H. Flexible multilayered MXene/thermoplastic polyurethane films with excellent electromagnetic interference shielding, thermal conductivity, and management performances. *Advx. Compos. Hybrid Mater.* **2021**, *4*, 274–285.
[78] Zhu, Y.; Zhao, X. B.; Peng, Q. Y.; Zheng, H. W.; Xue, F. H.; Li, P. Y.; Xu, Z. H.; He, X. D. Flame-retardant MXene/polyimide film with outstanding thermal and mechanical properties based on the secondary orientation strategy. *Nanoscale Adv.* **2021**, *3*, 5683–5693.
[79] Chu, Q. D.; Lin, H.; Ma, M.; Chen, S.; Shi, Y. Q.; He, H. W.; Wang, X. Cellulose nanofiber/graphene nanoplatelet/MXene nanocomposites for enhanced electromagnetic shielding and high in-plane thermal conductivity. *ACS Appl. Nano Mater.* **2022**, *5*, 7217–7227.
[80] Jiao, E. X.; Wu, K.; Liu, Y. C.; Lu, M. P.; Hu, Z. R.; Chen, B.; Shi, J.; Lu, M. G. Ultrarobust MXene-based laminated paper with excellent thermal conductivity and flame retardancy. *Compos. Part A Appl. Sci. Manuf.* **2021**, *146*, 106417.
[81] Wang, X. F.; Lei, Z. W.; Ma, X. D.; He, G. F.; Xu, T.; Tan, J.; Wang, L. L.; Zhang, X. S.; Qu, L. J.; Zhang, X. J. A lightweight MXene-coated nonwoven fabric with excellent flame retardancy, EMI shielding, and electrothermal/photothermal conversion for wearable heater. *Chem. Eng. J.* **2022**, *430*, 132605.
[82] Rasool, K.; Helal, M.; Ali, A.; Ren, C. E.; Gogotsi, Y.; Mahmoud, K. A. Antibacterial activity of $Ti_3C_2T_x$ MXene. *ACS Nano* **2016**, *10*, 3674–3684.
[83] Du, H. S.; Parit, M.; Liu, K.; Zhang, M. M.; Jiang, Z. H.; Huang, T. S.; Zhang, X. Y.; Si, C. L. Multifunctional cellulose nanopaper with superior water-resistant, conductive, and antibacterial properties functionalized with chitosan and polypyrrole. *ACS Appl. Mater. Interfaces* **2021**, *13*, 32115–32125.
[84] Zhang, C.; Liu, R. G.; Xiang, J. F.; Kang, H. L.; Liu, Z. J.; Huang, Y. Dissolution mechanism of cellulose in *N, N*-Dimethylacetamide/lithium chloride: Revisiting through molecular interactions. *J. Phys. Chem. B* **2014**, *118*, 9507–9514.